Submitted to Geophysics

LBL-7010
Preprint

RESISTIVITY MODELING FOR ARBITRARILY SHAPED THREE-DIMENSIONAL STRUCTURES

Abhijit Dey and H. Frank Morrison

October 1977

Prepared for the U. S. Department of Energy
under Contract W-7405-ENG-48

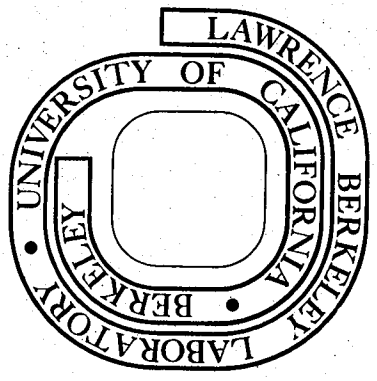

October 27, 1977
LBL: 7010

Resistivity Modeling for Arbitrarily Shaped Three-Dimensional Structures

Abhijit Dey

and

H. Frank Morrison

Engineering Geoscience
University of California
Berkeley

Abstract

A numerical technique has been developed to solve the three-dimensional potential distribution about a point source of current located in or on the surface of a half-space containing an arbitrary three-dimensional conductivity distribution. Self-adjoint difference equations are obtained for Poisson's equation using finite-difference approximations in conjunction with an elemental volume discretization of the lower half-space. Potential distribution at all points in the set defining the subsurface are simultaneously solved for multiple point sources of current. Accurate and stable solutions are obtained using full, banded, Cholesky decomposition of the capacitance matrix as well as the recently developed Incomplete Cholesky-Conjugate Gradient Iterative method.

A comparison of the two- and three-dimensional simple block-shaped models, for the collinear dipole-dipole array, indicates substantially lower anomaly indices for inhomogeneities of finite strike-extent. In general, the strike-extents of inhomogeneities have to be approximately 10 times the dipole lengths before the response becomes two-dimensional. The saturation effect with increasing conductivity contrasts appears sooner for the three-dimensional conductive inhomogeneities than for corresponding models with infinite strike lengths.

A downhole-to-surface configuration of electrodes produces diagnostic total field apparent resistivity maps for three-dimensional buried inhomogeneities. Experiments with various lateral and depth locations of the current pole indicate that mise a la masse surveys give the largest anomaly if a current pole is located asymmetrically and preferably near the top-surface of the buried conductor.

Introduction

Full utilization of the electrical resistivity method in geophysical prospecting has been limited by an inability to calculate the anomalies caused by specific structures. The widespread application of the d.c. resistivity and induced polarization methods as primary exploration tools coupled with developments in rapid, accurate, data acquisition techniques warrant more quantitative interpretation of the geologic structure than is currently practiced. In the past decade, substantial advances have been made in this direction through analog and numerical modeling techniques for two-dimensional geologic structures (e.g. , McPhar Geophysics, 1966, Madden, 1967, Coggon, 1971, Lee, 1975, Jepsen, 1969, Dey and Morrison, 1976). In complex geologic environments often encountered in geothermal and mineral exploration, however, even a two-dimensional portrayal of the structure is often inadequate and more complex solutions for three-dimensional distribution of resistivity must be sought.

Several solutions have been presented for the resistivity response of three-dimensional structures. Some analog scale modeling (McPhar Geophysics, 1966) has helped to understand the responses for a model suite of restricted physical dimensions and large conductivity contrasts. Numerical techniques using integral equation formulations have been developed by Dieter et al. (1969) and Bakbak (1977) for a single body located in a conductive half-space, and by Hohmann (1975) and Meyer (1977) for a single rectangular, prismatic inhomogeneity situated in a half-space with or without an isotropic overburden layer of uniform thickness. These new techniques provide valuable information for the interpretation of data obtained in simple geologic situations involving a single, laterally bounded inhomogeneity. In practice, however, the conductive targets occur as bodies of finite strike length, variable dip, and in the vicinity of faults, beneath overburden of variable thickness and conductivity. It

is, therefore, necessary to develop numerical modeling techniques to simulate structures with a totally arbitrary three-dimensional distribution of electrical conductivity.

In this paper a direct, explicit finite difference technique is employed to solve for the potential distribution due to a point source of current in or on the surface of a half-space with an arbitrary three-dimensional distribution of conductivity. The finite-difference scheme is chosen because of the inherent simplicity of the approximation forms which are also easily amenable to Dirichlet, Neumann, or mixed boundary conditions. Poisson's equation is discretized by elemental volumes over an irregularly-spaced three-dimensional prismatic grid. The unknown potential at all of the nodes in the grid are evaluated by using Successive Overrelaxation, Incomplete Cholesky - Conjugate Gradient and Direct Matrix Decomposition techniques to obtain accurate and stable solutions.

Using algebraic combinations of the potentials due to point current sources of opposite sign located inside or on the surface of the half-space, any arbitrary electrode configuration used in prospecting may be simulated. Results of certain surficial and down-hole electrode configurations employed over a number of three-dimensional structures are illustrated in the latter sections of this paper.

Fundamental Relations

Ohm's law relates the current density $\vec{J}$ to electric field intensity $\vec{E}$ and an isotropic conductivity σ by

$$\vec{J} = \sigma\vec{E}$$

Since stationary electric fields are conservative,

$$\vec{E} = -\nabla\phi \ ,$$

where ϕ is the electric potential.

Applying the principle of conservation of charge over a volume, and using the equation of continuity, we obtain

$$\nabla.\vec{J} = \partial\rho/\partial t\delta(x)\delta(y)\delta(z), \qquad (1)$$

where ρ is the charge density specified at a point in the cartesian x-y-z space by the Dirac delta function.

Equation (1) can be rewritten for a generalized three-dimensional space as

$$-\nabla.[\sigma(x,y,z)\nabla\phi(x,y,z)] = \partial\rho/\partial t\delta(x-x_s)\delta(y-y_s)\delta(z-z_s)\ , \qquad (2)$$

where (x_s, y_s, z_s) are the coordinates of the point source of injected charge.

Over an elemental volume ΔV about the charge injection point, the source term of equation (2) can be rewritten as

$$\partial\rho/\partial t\delta(x-x_s)\delta(y-y_s)\delta(z-z_s) = I/\Delta V\delta(x-x_s)\delta(y-y_s)\delta(z-z_s),$$

where I is the current in amperes.

Hence, equation (2) becomes

$$-\nabla.\ [\sigma(x,y,z)\nabla\phi(x,y,z)] = I/\Delta V\ \delta(x-x_s)\delta\ (y-y_s)\delta(y-y_s)\delta\ (z-z_s)\ . \qquad (3)$$

In this paper we will discuss methods for obtaining a numerical solution to equation (3) subject to the following boundary conditions:

1) $\phi(x,y,z)$ must be continuous across each boundary of the physical property distribution $\sigma(x,y,z)$ and
2) The normal component of $J(\equiv\sigma\partial\phi/\partial\eta)$ must also be continuous across

each boundary.

The solution of $\phi(x,y,z)$ is obtained by deriving the "difference equations" of (3) by a proper discretization of the (x,y,z) space over which the problem is to be solved.

Equation (3) is defined in a set $(x,y,z) \in R$ which is assumed to be closed and connected, to have a non-void interior and to have a sufficiently regular boundary Γ with outward normal η on which the boundary conditions are of the type

$$\alpha(x,y,z)\,\phi(x,y,z) + \beta(x,y,z)\frac{\partial\phi(x,y,z)}{\partial\eta} = f_2(x,y,z),\ (x,y,z) \in R \quad ,$$

with $\alpha(x,y,z) \geq 0;\ \beta(x,y,z) \geq 0;\ \alpha + \beta > 0$. (4)

In physical simulation, we also have the conductivity distribution function that is at least piecewise continuous in R and its closure, and which satisfies

$$\sigma(x,y,z) > 0,\ (x,y,z) \in R$$

Equation (3) is a self-adjoint, strongly connected and nonseparable elliptic equation of second order (Varga, 1962). The procedure of finite-difference discretization solves, numerically on a non-uniform rectangular prismatic mesh, the problem

$$L\phi(x,y,z) = -\nabla.[\sigma(x,y,z)\nabla\phi(x,y,z)] = I(x,y,z) \text{ on } R$$

subject to the boundary condition (4). The positivity of $\sigma(x,y,z)$ implies that

the operator L is positive definite.

(1) Discretization of the Three-Dimensional Resistivity Problem

To define the semi-infinite lower half-space with arbitrary conductivity distribution, the set R is designed with artificial boundaries simulating the infinitely distant planes in the horizontal (x- and y-directions) and the vertical (z-direction) extent. Such a lower half-space is illustrated by the grid shown in Figure 1. The grid is chosen to be a rectangular prism with arbitrary, irregular spacing of the nodes in the x, y and z directions. The nodes in the x-direction are indexed by $i = 1, 2, 3, \ldots L$; those in the y-direction by $j = 1, 2, 3, \ldots M$, and the nodes in the z-direction by $k = 1, 2, 3, \ldots N$, respectively. The infinitely distant planes at $x = -\infty$ and $+\infty$ are represented by the nodes on the faces with $i = 1$ and L, respectively. Similarly, the infinitely distant planes at $y = -\infty$ and $+\infty$ are simulated by the nodes on the faces with $j = 1$ and M, respectively and the bottom plane at $z = \infty$ is represented by the face with $k = N$. The primary potential due to a point source on a half-space, as well as the secondary perturbational potentials due to conductivity inhomogeneities in the lower half-space, fall inversely with the radial distance away from the source. Hence, by assigning large numbers for L, M, and N with suitable coarsening of the grid as $i \to 1$, $i \to L$, $j \to 1$, $j \to M$ and $k \to N$ and appropriate boundary conditions, the infinitely distant planes could be simulated by a finite choice of L, M and N.

Boundary Conditions Applied on the Edge, Γ, of the Region R

Since the simulation of the whole space is restricted to the conductive lower half-space alone in R, it is required that the boundary conditions be specified at points $(x,y,z) \in \Gamma \cup R$. At the ground surface with $z = 0$, this is implemented by applying the Neumann type condition

$\sigma_{i,j,k}\frac{\partial\phi_{i,j,k}}{\partial\eta} = 0$, for all i = 1,2,.....L; j = 1,2,3,....M with k = 1

The termination of the lower half-space at $x = \pm\infty$, $y = \pm\infty$ and $z = +\infty$ is done by extending the mesh far enough away from the sources and conductivity inhomogeneities such that the total potential distribution at these planes approaches asymptotic values. The boundary values at these "infinitely distant planes" can be specified from known solutions of homogeneous or layered primary distribution of conductivity. Inhomogeneities are viewed as perturbations over this distribution. If these values are specified at all nodes on the infinitely distant planes, the boundary conditions on Γ become Dirichlet type. In the general case of simulation of arbitrary conductivity distribution, often a suitable primary model solution cannot be analytically computed. In such cases either i) the total potential at these planes are assumed to be zero (Dirichlet Condition) or ii) at these planes $\sigma_{i,j,k}\frac{\partial\phi_{i,j,k}}{\partial\eta}$ is assumed to be zero (Neumann Condition). It is often found that the first assumption causes an undershoot and the second assumption causes an overshoot in the numerically evaluated potentials beginning at some distance from the point source (Coggon,1971) when compared with analytic solutions.

In this paper, a mixed boundary condition is proposed for the infinitely distant planes at $x = \pm\infty$, $y = \pm\infty$ and $z = \infty$, using the asymptotic behaviour of $\phi(x,y,z)$ and $\frac{\partial\phi(x,y,z)}{\partial\eta}$ at large distances from the source point. The total potential at large distances from the source as well as inhomogeneities have the general form of

$$\phi(x,y,z) \simeq \frac{A}{\sqrt{x^2 + y^2 + z^2}} = \frac{A}{r}, \quad (A = \text{constant})$$

Hence

$$\frac{\partial\phi(x,y,z)}{\partial\eta} = -\frac{A}{r^2}\hat{e}_r.\hat{\eta} = -\frac{\phi(x,y,z)}{r}.\cos\theta$$

where θ is the angle between the radial distance r and the outward normal η. We can, therefore, rewrite equation (4) as

$$\frac{\partial\phi(x,y,z)}{\partial\eta} + \frac{\alpha\phi(x,y,z)}{r} = 0 \qquad (5)$$

with $\alpha = \cos\theta$

Such a mixed boundary condition takes advantage of the physical behaviour of the potential at the distant bounding planes and does not require an a priori assumption of the nature of ϕ or $\frac{\partial\phi}{\partial\eta}$ that are to be evaluated in terms of a primary conductivity structure. It also has the inherent advantage of reducing the amount of coarsening of the grid required as the bounding planes are approached and reflections due to the virtual sources along the edge nodes are simultaneously eliminated.

Discretization by Elemental Volume

The physical property distribution $\sigma_{i,j,k}$ at any node (i,j,k) of the prismatic grid (as shown in Figure 1) is discretized such that $\sigma_{i,j,k}$ represents the conductivity of a volume enclosed by the nodes i,j,k; i + 1, j, k; i, j + 1, k; i + 1, j + 1, k; i, j, k + 1; i + 1, j, k + 1; i, j + 1, k + 1 and i + 1, j + 1, k + 1. The numerical solution of equation (3) that consists of a discretized set of $\phi_{i,j,k}$ at each node, is to be evaluated. The node (i,j,k) is assumed to represent the closed mesh region $\Delta V_{i,j,k}$ about the node as shown in Figure 1. It is seen that for a nodal point in the interior,

$$\Delta V_{i,j,k} = \frac{(\Delta x_i + \Delta x_{i-1}) \cdot (\Delta y_j + \Delta y_{j-1}) \cdot (\Delta z_k + \Delta z_{k-1})}{8}$$

and in the limit as $z \to 0$, for a nodal point on the ground surface,

$$\Delta V_{i,j,k} = \frac{(\Delta x_i + \Delta x_{i-1}) \cdot (\Delta y_j + \Delta y_{j-1}) \cdot \Delta z_k}{8}$$

For each node (i,j,k) for which $\phi_{i,j,k}$ is unknown, we now integrate equation (3) over the corresponding elemental volume $\Delta V_{i,j,k}$ to obtain

$$-\iiint_{\Delta V_{i,j,k}} \nabla.\left[\sigma(x,y,z)\nabla\phi(x,y,z)\right] dx_i dy_j dz_k = \iiint_{\Delta V_{i,j,k}} \frac{I}{\Delta V_{i,j,k}} .\delta(x_i-x_s)\delta(y_j-y_s)\delta(z_k-z_s)\, dx_i dy_j dz_k$$

$$= I\delta(x_i-x_s)\delta(y_j-y_s)\delta(z_k-z_s) . \qquad (6)$$

Using Green's theorem, the volume integral becomes

$$\iiint_{\Delta V_{i,j,k}} \nabla.(\sigma\nabla\phi)dv = \iint_{S_{i,j,k}} \sigma \frac{\partial\phi}{\partial\eta} ds , \qquad (7)$$

and equation (6) is rewritten as

$$\iint_{S_{i,j,k}} \sigma(x,y,z) \frac{\partial\phi(x,y,z)}{\partial\eta} ds_{i,j,k} = I\delta(x_i-x_s)\delta(y_j-y_s)\delta(z_k-z_s) , \qquad (8)$$

where η is the outward normal and $S_{i,j,k}$ is the surface enclosing the elemental volume $\Delta V_{i,j,k}$. It is seen from equation (7) that over every element of R and on the boundary Γ, the boundary conditions given by equation (5) can be directly implemented in the left hand side of equation (8).

The surface integral in equation (8) along the bounding surface $S_{i,j,k}$ is subdivided into six subsurfaces as indicated in Figure 2. For an interior node in the discretization grid, by approximating $\frac{\partial\phi}{\partial\eta}$ by central difference and integrating along each of the bounding faces of the elemental volume, $\Delta V_{i,j,k}$

we get,

$$\iint_{S_{i,j,k}} \sigma_{i,j,k} \cdot \frac{\partial \phi_{i,j,k}}{\partial \eta} \, ds_{i,j,k}$$

$$= \frac{\phi_{i,j-1,k} - \phi_{i,j,k}}{\Delta y_{j-1}} \left[\sigma_{i-1,j-1,k-1} \frac{\Delta z_{k-1} \, \Delta x_{i-1}}{4} + \sigma_{i,j-1,k-1} \frac{\Delta z_{k-1} \, \Delta x_i}{4} + \sigma_{i-1,j-1,k} \cdot \frac{\Delta x_{i-1} \Delta z_k}{4} + \sigma_{i,j-1,k} \frac{\Delta x_i \Delta z_k}{4} \right]$$

$$+ \frac{\phi_{i,j+1,k} - \phi_{i,j,k}}{\Delta y_j} \left[\sigma_{i-1,j,k-1} \frac{\Delta z_{k-1} \cdot \Delta x_{i-1}}{4} + \sigma_{i,j,k-1} \frac{\Delta z_{k-1} \cdot \Delta x_i}{4} + \sigma_{i-1,j,k} \frac{\Delta x_{i-1} \cdot \Delta z_k}{4} + \sigma_{i,j,k} \frac{\Delta x_i \Delta z_k}{4} \right]$$

$$+ \frac{\phi_{i+1,j,k} - \phi_{i,j,k}}{\Delta x_i} \left[\sigma_{i,j-1,k-1} \frac{\Delta y_{j-1} \cdot \Delta z_{k-1}}{4} + \sigma_{i,j,k-1} \frac{\Delta y_j \cdot \Delta z_{k-1}}{4} + \sigma_{i,j-1,k} \frac{\Delta y_{j-1} \cdot \Delta z_k}{4} + \sigma_{i,j,k} \frac{\Delta y_j \Delta z_k}{4} \right]$$

$$+ \frac{\phi_{i-1,j,k} - \phi_{i,j,k}}{\Delta x_{i-1}} \left[\sigma_{i-1,j-1,k-1} \frac{\Delta y_{j-1} \cdot \Delta z_{k-1}}{4} + \sigma_{i-1,j,k-1} \frac{\Delta y_j \Delta z_{k-1}}{4} + \sigma_{i-1,j-1,k} \right.$$

$$\cdot \frac{\Delta y_{j-1}\Delta z_k}{4} + \sigma_{i-1,j,k}\frac{\Delta y_j \Delta z_k}{4}\Bigg]$$

$$+\left(\frac{\phi_{i,j,k-1} - \phi_{i,j,k}}{\Delta z_{k-1}}\right)\Bigg[\sigma_{i-1,j,k-1}\frac{\Delta x_{i-1}\Delta y_j}{4} + \sigma_{i,j,k-1}\frac{\Delta x_i \Delta y_j}{4} + \sigma_{i-1,j-1,k-1}\frac{\Delta x_{i-1}\cdot\Delta y_{j-1}}{4}$$

$$+ \sigma_{i,j-1,k-1}\frac{\Delta x_i \Delta y_{j-1}}{4}\Bigg]$$

$$+\left(\frac{\phi_{i,j,k+1} - \phi_{i,j,k}}{\Delta z_k}\right)\Bigg[\sigma_{i-1,j,k}\frac{\Delta x_{i-1}\cdot\Delta y_j}{4} + \sigma_{i,j,k}\frac{\Delta x_i \Delta y_j}{4} + \sigma_{i-1,j-1,k}\frac{\Delta x_{i-1}\Delta y_{j-1}}{4}$$

$$+ \sigma_{i,j-1,k}\frac{\Delta x_i \Delta y_{j-1}}{4}\Bigg] \quad . \tag{9}$$

Substituting equation (9) in (8), we obtain, for an interior node (i,j,k), the discretized equation

$$C^{ijk}_{top}\cdot\phi_{i,j,k-1} + C^{ijk}_{bottom}\cdot\phi_{i,j,k+1} + C^{ijk}_{left}\cdot\phi_{i-1,j,k} + C^{ijk}_{right}\cdot\phi_{i+1,j,k} + C^{ijk}_{front}\cdot\phi_{i,j-1,k}$$

$$+ C^{ijk}_{back}\cdot\phi_{i,j+1,k} + C^{ijk}_{p}\cdot\phi_{i,j,k} = I\delta(x_i-x_s)\delta(y_j-y_s)\delta(z_k-z_s)\,, \tag{10}$$

where C^{ijk}_{top} = coupling coefficient between the nodes (i,j,k) and (i,j,k-1)

$$= \frac{-1}{\Delta z_{k-1}}\Bigg[\sigma_{i-1,j,k-1}\frac{\Delta x_{i-1}\Delta y_j}{4} + \sigma_{i,j,k-1}\frac{\Delta x_i \Delta y_j}{4} + \sigma_{i-1,j-1,k-1}\frac{\Delta x_{i-1}\Delta y_{j-1}}{4} + \sigma_{i,j-1,k-1}$$

$$\cdot \frac{x_i\, y_{j-1}}{4} \Bigg\}, \qquad \text{- (10.1)}$$

C^{ijk}_{bot} = coupling coefficient between the nodes (i,j,k) and (i,j,k + 1)

$$= -\frac{1}{\Delta z_k}\left\{\sigma_{i-1,j,k}\frac{\Delta x_{i-1}\Delta y_j}{4} + \sigma_{i,j,k}\frac{\Delta x_i \Delta y_j}{4} + \sigma_{i-1.j-1,k}\frac{\Delta x_{i-1}\Delta y_{j-1}}{4} + \sigma_{i,j-1,k} \cdot \frac{\Delta x_i \Delta y_{j-1}}{4}\right\}, \qquad \text{- (10.2)}$$

C^{ijk}_{left} = coupling coefficient between the nodes (i,j,k) and (i-1,j,k)

$$= -\frac{1}{\Delta x_{i-1}}\left\{\sigma_{i-1,j-1,k-1}\frac{\Delta y_{j-1}\Delta z_{k-1}}{4} + \sigma_{i-1,j,k-1}\frac{\Delta y_j \Delta z_{k-1}}{4} + \sigma_{i-1,j-1,k}\frac{\Delta y_{j-1}\Delta z_k}{4} + \sigma_{i-1,j,k}\frac{\Delta y_j \Delta z_k}{4}\right\}, \qquad \text{- (10.3)}$$

C^{ijk}_{right} = coupling coefficient between the nodes (i,j,k) and i+1,j,k)

$$= -\frac{1}{\Delta x_i}\left\{\sigma_{i,j-1,k-1}\frac{\Delta y_{j-1}\Delta z_{k-1}}{4} + \sigma_{i,j,k-1}\frac{\Delta y_j \Delta z_{k-1}}{4} + \sigma_{i,j-1,k}\frac{\Delta y_{j-1}\Delta z_k}{4} + \sigma_{i,j,k} \cdot \frac{\Delta y_j \Delta z_k}{4}\right\}, \qquad \text{- (10.4)}$$

C^{ijk}_{front} = coupling coefficient between the nodes(i,j,k) and (i,j-1,k)

$$= -\frac{1}{\Delta y_{j-1}}\left\{\sigma_{i-1,j-1,k-1}\frac{\Delta x_{i-1}\Delta z_{k-1}}{4} + \sigma_{i,j-1,k-1}\frac{\Delta x_i \Delta z_{k-1}}{4} + \sigma_{i-1,j-1,k}\frac{\Delta x_{i-1}\Delta z_k}{4}\right.$$

$$+ \sigma_{i,j-1,k} \frac{\Delta x_i \Delta z_k}{4} \Bigg] \quad , \qquad \text{-(10.5)}$$

C^{ijk}_{back} = coupling coefficient between the nodes(i,j,k) and (i,k+1,k)

$$= \frac{-1}{\Delta y_j} \Bigg[\sigma_{i-1,j,k-1} \frac{\Delta x_{i-1} \Delta z_{k-1}}{4} + \sigma_{i,j,k-1} \frac{\Delta x_i \Delta z_{k-1}}{4} + \sigma_{i-1,j,k} \frac{\Delta x_{i-1} \Delta z_k}{4} + \sigma_{i,j,k} \cdot \frac{\Delta x_i \Delta z_k}{4} \Bigg] \quad , \qquad \text{-(10.6)}$$

and C^{ijk}_{p} = self coupling coefficient at node (i,j,k)

$$= - \left[C^{ijk}_{top} + C^{ijk}_{bottom} + C^{ijk}_{left} + C^{ijk}_{right} + C^{ijk}_{front} + C^{ijk}_{back} \right] \qquad (10.7)$$

The self-adjoint difference equation (10) indicates that the solution ϕ at the (i,j,k) node is dependent only on the values of ϕ at the adjacent nodes (i,j,k-1), (i,j,k+1), (i-1,j,k), (i+1,j,k), (i,j-1,k) and (i,j+1,k). The node coupling coefficients are known functions of the geometry and predefined physical property distribution at all nodes in the set R.

The difference equations for the nodes located on the 'infinitely distant' edge Γ of the set R are somewhat altered from that of an interior node, since the asymptotic mixed boundary condition is to be implemented at these node locations. At all nodes on the ground surface (z = 0), the Neumann condition is implemented as $\sigma \frac{\partial \phi}{\partial z} = 0$. For all other nodes located on the remaining faces, edges and corners, the mixed boundary condition $\sigma \frac{\partial \phi}{\partial z} = - \frac{\sigma \phi}{r} \cos\theta$ (from equation (5)) is directly

implemented while integrating over the appropriate bounding surfaces, for the outward normal η oriented, in the x-, y-, or z- directions. For brevity, the modified difference equations for only two typical locations of nodes on Γ are illustrated in the following.

Coupling coefficients for the difference equation (10) modified for a node (i,j,k) located on the bottom face (excluding the edges and corner locations on this plane) of the grid is given as

$$C^{ijk}_{top} = -\frac{1}{\Delta z_{k-1}}\left\{\sigma_{i-1,j,k-1}\frac{\Delta x_{i-1}\Delta y_j}{4} + \sigma_{i,j,k-1}\frac{\Delta x_i \Delta y_j}{4} + \sigma_{i-1,j-1,k-1}\frac{\Delta x_{i-1}\Delta y_{j-1}}{4} + \sigma_{i,j-1,k-1}\frac{\Delta x_{j-1}\Delta y_{j-1}}{4}\right\},$$

$$C^{ijk}_{bottom} = 0.0,$$

$$C^{ijk}_{left} = -\frac{1}{\Delta x_{i-1}}\left\{\sigma_{i-1,j-1,k-1}\frac{\Delta y_{j-1}\Delta z_{k-1}}{4} + \sigma_{i-1,j,k-1}\frac{\Delta y_j \Delta z_{k-1}}{4}\right\},$$

$$C^{ijk}_{right} = -\frac{1}{\Delta x_i}\left\{\sigma_{i,j-1,k-1}\frac{\Delta y_{j-1}\Delta z_{k-1}}{4} + \sigma_{i,j,k-1}\frac{\Delta y_j \Delta z_{k-1}}{4}\right\},$$

$$C^{ijk}_{front} = -\frac{1}{\Delta y_{j-1}}\left\{\sigma_{i-1,j-1,k-1}\frac{\Delta x_{i-1}\Delta z_{k-1}}{4} + \sigma_{i,j-1,k-1}\frac{\Delta x_i \Delta z_{k-1}}{4}\right\},$$

$$C^{ijk}_{back} = -\frac{1}{\Delta y_j}\left\{\sigma_{i-1,j,k-1}\frac{\Delta x_{i-1}\Delta z_{k-1}}{4} + \sigma_{i,j,k-1}\frac{\Delta x_i \Delta z_{k-1}}{4}\right\},$$

$$C^{ijk}_{p} = -\left[C^{ijk}_{top} + C^{ijk}_{left} + C^{ijk}_{right} + C^{ijk}_{front} + C^{ijk}_{back} \right] - C^{ijk}_{top} \cdot \frac{|z_s - z_k| \Delta z_{k-1}}{r}$$

where r is the radial distance from the source point to the node (i,j,k).

Similarly, the coupling coefficients for a node (i,j,k) located on Γ at the top, back, right corner of the discretization grid are derived as

$$C^{ijk}_{top} = C^{ijk}_{back} = C^{ijk}_{right} = 0.0 \quad ,$$

$$C^{ijk}_{bottom} = -\sigma_{i-1,j-1,k} \frac{\Delta x_{i-1} \Delta y_{j-1}}{4 \Delta z_k} \quad ,$$

$$C^{ijk}_{left} = -\sigma_{i-1,j-1,k} \frac{\Delta y_{j-1} \Delta z_k}{4 \Delta x_{i-1}} \quad ,$$

$$C^{ijk}_{front} = -\sigma_{i-1,j-1,k} \frac{\Delta x_{i-1} \Delta z_k}{4 \Delta y_{j-1}} \quad ,$$

and

$$C^{ijk}_{p} = -\left[C^{ijk}_{bottom} + C^{ijk}_{left} + C^{ijk}_{front} \right] - \left[C^{ijk}_{bottom} \frac{|z_s - z_k| \cdot \Delta z_k + C^{ijk}_{left} \cdot |x_s - x_i| \cdot \Delta x_{i-1}}{r^2} + \frac{C^{ijk}_{front} |y_j - y_s| \cdot \Delta y_{j-1}}{r^2} \right] .$$

In applying the mixed boundary condition at the nodes located on the edge Γ, the radial distance to all the relevant nodes may be evaluated from the central point on the top surface of the prismatic mesh. While for different source locations the corresponding radial distances are slightly different, in the asymptotic limit, at Γ, no substantial error arises from this assumption. This assumption also enables the coupling coefficients thus generated to be invariant for any arbitrary source location. It is found experimentally that this mixed boundary condition at the edges of the grid produces a solution for ϕ that allows a considerably better fit to the analytically computed solution at large distances from the source location.

Matrix Formulation

The self-adjoint difference equation (10) is obtained for each node in the set R, once the appropriate coupling coefficients are derived using the proper boundary conditions. The set of difference equations for each node are then assembled into a global or capacitance matrix form. In the course of the assembly each node is numbered in an order to minimize the bandwidth of the matrix (Zienkiewiez, 1971). The set of simultaneous equations for all the nodes in the grid can be written symbolically as

$$[C]\,[\phi] = [S] \tag{11}$$

where C is an LMN X LMN matrix, called the capacitance matrix and is a function only of the geometry and the physical property distribution in the grid. The vector ϕ consists of the unknown solutions of the total potential at all the nodes and the vector S contains the source terms of charge injection. It is to be noted that for multiple source locations, the C-matrix remains unaltered and a single decomposition of this matrix provides solutions for multiple S vectors, through repeated backsubstitutions.

The capacitance matrix C has the following properties:

i) $C_{pp} > 0$, p = 1, 2, 3 . . . LMN ,

ii) $C_{pp} \geq \sum_{\substack{q=1 \\ q \neq p}}^{LMN} |C_{p,q}|$, p = 1, 2, . . . LMN,

i.e. C is diagonally dominant ,

iii) C is symmetric, sparse and banded with only six non-zero co-diagonals ,

iv) C is irreducible and has a strongly connected graph (Varga, 1962), and

v) C possesses Young's Property A (Young, 1954).

It has been shown by Varga (1962) that the explicit difference equations that give rise to the matrix C with properties described above, are inherently stable for irregular grid spacings.

Solution of the Matrix Equation

In realistic simulations of the geologic models for electrical resistivity applications, the descretization grid generally results in 10,000 - 15,000 nodes at which the total potentials are to be evaluated for multiple current injection points. Such discretizations result in matrices that are rather unwieldy to handle even on a very large and fast machine (e.g. a CDC 7600). We have attempted to solve such systems of equations using i) Successive Over-relaxation methods, ii) Incomplete Cholesky-Conjugate Gradient method and iii) Banded Matrix Decomposition techniques.

Equation (11) results in a very sparse banded matrix that has been traditionally solved using Successive Point Overrelaxation (Southwell, 1946) or Alternating Direction Iterative methods (e.g. Varga; 1962, Douglass and Rachford; 1956; Gunn, 1964). In these methods, an initial assumed distribution of ϕ_{ijk} over the grid is relaxed by successive refinements through iterations. The refinements in individual methods are either in terms of individual nodes,

rows or columns of nodes or of ϕ_{ijk} alternately along a column and a row. The refinement obtained upon an iteration is further updated by the use of an optimal overrelaxation factor or by successive use of the Chebychev over-relaxation acceleration parameter (Concus and Golub, 1973). In the large grids under consideration ($\sim$10,000 - 15,000 nodal points), the successive overrelaxation and the alternating direction iterative techniques (Doss, 1977) require a minimum of 200 - 300 iteration sweeps through the entire grid for each location of the point source of current injection to produce solutions to an accuracy of 1% to 5%. In addition, the convergence rates of these iterative techniques are highly dependent on the dimensions of the grid spacings and the nature of the physical property distributions. Although the operation counts per iteration in these methods are relatively small ($\sim$ 7 LMN to 15 LMN multiplications @ 0.3 to 1 seconds of CP time on CDC 7600), the reliability of an acceptable convergence level and reciprocity checks for arbitrary conductivity distributions were often very poor.

A new iterative method called the Incomplete Cholesky-Conjugate Gradient ICCG method for the solution of large, sparse systems of linear equations has been proposed by Meijerink and van der Vorst (1976). This method, when applied to the solution of large systems of elliptic partial differential equations, produces highly convergent solutions 10 - 100 times faster than the traditional Successive Overrelaxation or Alternating Direction Iterative methods (Kershaw, 1977). The conjugate-gradient method as originally proposed by Hestenes and Stiefel (1952) when applied directly to solve for very large, sparse systems with a high condition number ($\lambda max/\lambda min \equiv$ 10 to 100) is not very effective as an iterative method. However, in combination with an incomplete Cholesky de-composition of the C matrix, the iterative scheme is shown to be very efficient

(Meijerink and van der Vorst, 1976).

In standard Cholesky decomposition, the symmetric, positive definite matrix C is written as

$$C = LL^T$$

where L is lower triangular. With this decomposition of C, the equation $C\phi = S$ is easily solved as $\phi = (L^T)^{-1}\ (L^{-1}S)$. In practice, however, for a sparse matrix C, the L-matrix is full and is time consuming to generate in its entirety. In the Incomplete Cholesky - Conjugate gradient method an approximate decomposition of C is made such that

$$C = LL^T + E \quad (E = \text{Error term})$$

with the new factorized L-matrix having the same sparsity pattern imposed on it as the original C-matrix (ICCG (0), Ref. Meijerink and van der Vorst, 1976). With the new approximation of $(LL^T)^{-1}$ for C^{-1}, $L^{-1}C(L^T)^{-1}$ will be an approximate identity matrix and the conjugate-gradient method applied to the matrix $L^{-1}C(L^T)^{-1}$ converges very rapidly. The solution of the system of equations $C\phi = S$ then is iteratively refined as indicated in the following algorithm (Kershaw, 1977):

Let $r_0 = S - C\phi_0$ and $p_0 = (LL^T)^{-1}\ r_0$,

ϕ_0 being any arbitrary assumed vector ,

then

$$a_i = \frac{\langle r_i,\ (LL^T)^{-1}\ r_i\rangle}{\langle p_i,\ Cp_i\rangle}$$

$$\phi_{i+1} = \phi_i + a_i p_i$$

$$r_{i+1} = r_i - a_i C p_i$$

$$b_i = \frac{\langle r_i + 1,\ (LL^T)^{-1} r_i + 1 \rangle}{\langle r_i, (LL^T)^{-1} r_i \rangle}$$

$$p_i + 1 = (LL^T)^{-1} r_i + 1 + b_i p_i$$

where the subscript i indicates the iteration cycle.

The efficiency of the method depends on the validity of the approximation of $(LL^T)^{-1}$ for C^{-1}. The self-adjoint equations of the difference form couple a node most strongly to its nearest adjacent nodes. Eliminating distant co-diagonals in L, thus neglecting coupling to more distant nodes, is a good approximation. The operation count of such an iteration cycle is approximately 16 LMN multiplications ($\sim$1 second of CP time on the CDC 7600 per iteration for a system of 12000 equations). In the problem posed in our paper, this method yields a solution with 1% to 3% accuracy for a large grid system ($\sim$ 12000 nodes) in about 30 - 40 iterations per source location. In our experiments, this method has given adequately accurate results and is recommended when the total potential solutions in the entire mesh need to be solved for only a few (1 to 5) current source locations.

The third method that has been used to solve the large, sparse system is based on a full-banded decomposition of the Cholesky type. The symmetric triangular decomposition of the banded C-matrix is done in blocks using highly efficient random disk access facilities and auxilliary out-of-core storage devices (Reid, 1972; Wilson et al., 1974). For a symmetric matrix system of 11,628 equations and a half-band-width of 205 the decomposition process requires about 230 seconds of CP time on the CDC 7600 and the back-substitution for each of the multiple source vectors requires approximately 7 seconds of CP time. In our experiments, this method has yielded the most accurate and stable

solution independent of the irregular mesh geometry or the physical property distributions. The economics of computation with this method to generate dipole-dipole or pole-dipole pseudo-sections (with 13 - 15 source vectors) is competitive with that of Incomplete Cholesky-Conjugate Gradient method and is preferred because of its inherent stability and high degree of accuracy.

The recent advances in solving very large and very sparse systems using minimal degree ordering in conjunction with the nested dissection algorithms that take advantage of the non-zero element structure of the capacitance matrix (e.g. George and Liu; 1976; Reid; 1976; Sherman, 1975) will provide significantly more efficient solution techniques than the band or envelope methods hitherto used.

Determination of the Apparent Resistivity

In electrical resistivity surveys a current source +I and a current sink -I are used to energize the conductive earth. A potential difference, ΔV, is measured between two points located at arbitrary azimuthal orientations (for surface arrays) or colatitudinal configurations (as in down-hole-surface arrays). A parameter "Apparent Resistivity" is defined as a function

$$\rho_a = G \frac{\Delta V}{I}$$

where, for the configuration illustrated in Figure 3,

$$G = 2\pi \frac{1}{(1/r_1 - 1/r_2 - 1/r_3 + 1/r_4)} .$$

For a homogeneous half-space, ρ_a, is the true intrinsic resistivity of the medium. If, however, the lower semi-infinite medium has an inhomogeneous three-dimensional conductivity distribution, ρ_a, indicates the resistivity of an apparent homogeneous half-space that results in an identical ΔV for the transmitter-receiver locations under consideration. All interpretations of electrical resistivity work are done using the apparent resistivity concept described above.

It can be seen that the d.c. potential distribution at any point is the superposition of the solutions of two point sources of current located at the transmitting electrodes of amplitude +I and -I (the transmitting dipole).

Model Computations

In most of the results presented in this paper a rectangular prismatic grid with 57 x 17 x 12 (11,628) nodes was used. In the central shallow part of the mesh, the nodes were finely spaced to provide a maximum resolution of one quarter of the dipole length (used as an arbitrary unit distance) in the x-,y-, or z-direction for the model dimensions. To estimate the accuracy of the technique described in the previous sections, a two-layered earth model was simulated. The resistivity of the top layer of unit thickness was assumed to be 100 ohm-m and that of the bottom layer to be 10 ohm-m. A collinear dipole-dipole array was deployed with unit dipole length and with dipole separations N = 1, 2, 3 . . . 10. The numerical results are shown in Figure 4 with circles and the analytically computed response for the model is shown with a solid line. It can be seen that the numerical results approach the analytic solution with an absolute accuracy of better than 5%. Further tests made with analytical solutions for an outcropping contact, buried conductive sphere and with numerical solutions for block-shaped buried three-dimensional inhomogeneities (Meyer, 1977 and Bakbak, 1977) generally indicated good agreement, with an absolute accuracy in the range of 3 - 10%.

Model Results

A) Dipole-dipole Configuration

A series of models have been used in the following analysis to illustrate the effects of strike-length, depth of burial, conductivity contrast, and a conductive overburden layer for a single conductive inhomogeneity located in a dissipative half-space. A standard test model was chosen with dimensions

1 x 2 x 2 in the x, y, and z directions, respectively.

The surrounding host rock is assumed to have a resistivity of 100 ohm-m and the inhomogeneity is assigned a resistivity of 3 ohm-m.

i) Effect of the Strike Length

a) Without Conductive Overburden Layer

The apparent resistivity pseudo-sections along a profile line on the surface oriented normal to the strike of the inhomogeneity are shown in Figures 5a, 5b, 5c, 5d, 5e for strike lengths of 1, 2, 4, 6, and 10 units, respectively. The profile line bisects the strike-length in each case. The pseudo-section for the same inhomogeneity with infinite strike length is shown in Figure 5f. For strike lengths up to about 6 units, the most remarkable feature is the appearance of a relative apparent resistivity 'high' directly below the location of the inhomogeneity. The values here are larger than the resistivity of the surrounding medium, and this zone underlies a zone of low apparent resistivities observed at smaller dipole-separations. This feature has also been observed by Dieter et al. (1969) and Bakbak (1977). As the strike length is increased, the flanking 'high' zones grow in amplitude, while the 'high' directly below the location of the inhomogeneity decreases in amplitude. The zone of low apparent resistivities is best described by noting the progression of the 80 ohm-m contour in Figures 5a to 5f as the strike length is increased. The low resistivity zone increases in size and the values decrease from approximately 20% below the half-space value to over 50% in the case of the infinite strike length. With the strike length of about 10 units, the pseudo-section closely resembles that of a two-dimensional inhomogeneity in both pattern and amplitude.

b) With a Conductive Overburden Layer

The effect of varying strike lengths of the standardized inhomogeneity when it is overlain by a conductive overburden of thickness 0.5 units and

resistivity 10 ohm-m is illustrated in Figures 6a, 6b, 6c for strike lengths of 2, 6 units and infinity, respectively. The conductive overburden decreases the anomaly amplitude of the resistivity low substantially. The horizontal spreading of the current lines due to the screening effect of the conductive overburden causes the three-dimensional model values to approach the two-dimensional values for a strike length of only 6 units. At large dipole-separations, N = 7, 10, for a strike length of 2 units, the apparent resistivity values are somewhat higher than those from the two-dimensional model.

Unlike the case without overburden, the difference in the response pattern between the three- and two-dimensional models is much less. Were the low resistivity block of Figure 6c to be more deeply buried or less conductive the anomaly would in all practical cases be indistinguishable from the three-dimensional block of Figure 6a, which has a strike length of only 2 units.

ii) Effect of Depth of Burial

Figures 7 and 5b illustrate the apparent resistivity pseudo-sections for the standardized conductive inhomogeneity with depths of 0.5 and 1.0 units, respectively. The low resistivity anomaly associated with the body shows a sharp drop in amplitude with increasing depth of burial. The anomalous resistivity 'high' observed directly below the body at large dipole-separations grows in amplitude as the top of the inhomogeneity approaches the ground surface.

A conductive overburden layer of thickness 0.5 unit and resistivity 10 ohm-m overlies the standardized inhomogeneity with depths of burial of 0.5 units and 1 unit in Figures 8 and 6a, respectively. The anomaly patterns are considerably more diagnostic for the shallower depth to the top of the body although the anomaly amplitude is not very large. In our model studies, the response of such a conductive target appears to be indistinguishable from the two-layered

earth response for depths of burial greater than 1.5 units.

A summary of the effects of depth of burial and conductivity contrasts of the standardized three-dimensional body together with a two-dimensional model of identical cross-section is shown in Figure 9. A normalized anomaly index (AI) is defined as

$$AI = \frac{a^{max} - a^{min}}{background} \times 100\%$$

In the pseudo-sections of apparent resistivity there appear zones of relatively high as well as low values, due to the presence of a conductive target. The anomaly index (AI) is a measure of the distortion in the half-space response caused by the inhomogeneity. In the characteristic diagram, the AI measure shows substantially higher distortion for two-dimensional targets compared to the three-dimensional targets of identical cross-section for various conductivity contrasts. With increased depth of burial, the rate of drop in the anomaly level for both two- and three-dimensional bodies is approximately the same, although for comparable depths of burial the three-dimensional targets have much lower detectability.

It is also interesting to note that the AI of three-dimensional bodies show a saturation for contrasts in excess of 30. The AI for the two-dimensional case is still rising for a contrast of 100.

Profile Lines Shifted Along the Strike Direction.

The strike-extent of a three-dimensional inhomogeneity could be mapped by observations made along parallel profile lines normal to the strike. For the standardized inhomogeneity, this effect is shown in pseudo-sections illustrated in Figures 6b, 10a, 10b and 10c for line shifts of 0.0, 0.5, 1.0, 3.0 units from the center of the surface projection of the inhomogeneity. The patterns in the apparent resistivity pseudo-sections do not alter appreciably, for y = 0

(line bisecting the strike length) and y = 0.5. For the line at y = 1.0 unit (along the surface projection of one edge of the body), the resistivity 'low' zones shrinks laterally in the profiles, while the basic pattern is maintained. For the line at y = 3.0 units (Figure 10c) the effect of the inhomogeneity is substantially reduced in that a small anomaly of the order of 5% indicates the presence of a conductive target on one side of the profile.

Very similar patterns are observed for these lines when the standardized inhomogeneity is overlain by a conductive overburden layer.

With only one profile line, say that of Figure 10c, it would be impossible to deduce whether a conductive inhomogeneity was buried directly beneath the line or off to one side.

A. Basin and Range Geothermal Model

An analysis of a more complicated model has arisen from a field study of the geothermal potential in a typical Basin and Range geologic section. In such sections, the sediments are typically separated by steep normal faults from more resistive bedrock of the adjacent ranges. The bounding faults are hypothesized to be conduits for ascending hot water. Portions of the sedimentary section adjacent to the fault could act as reservoirs for hot water. To date, modeling used in the interpretation of resistivity surveys has considered only reservoirs of infinite strike length. It is probable, however, that only certain portions of the fault act as conduits so that the resulting reservoir would have limited strike length.

To assess the effectiveness of the resistivity method in such cases we have analyzed the responses of the three dimensional model described in Figures 11a and b. Six profile lines oriented parallel and perpendicular to the strike are indicated in the plan view (Figure 11a). The conductivity section on the line through the center of the body and perpendicular to

strike is shown in Figure 11b. Pseudo sections of apparent resistivities on these lines are shown in Figures 12a to 12f.

Two additional pseudo sections along line 1 are shown for the fault model with no conductivity inhomogeneity and with a conductive inhomogeneity of infinite strike length. (Figures 13 and 14, respectively). The most striking result is that for line 1 on a profile perpendicular to strike, the anomaly caused by the three-dimensional inhomogeneity is considerably less than its two-dimensional counterpart. The two-dimensional conductive reservoir (Figure 13) could be easily delineated, but the pseudo sections of Figure 12a could be interpreted as a sloping fault contact displaced somewhat to the left of its actual position. The anomaly patterns in the pseudo sections of lines 1, 2 and 3, and for the pseudo section of Figure 14, are very similar. Each could be interpreted as a fault contact with only subtle differences in location and dip.

For the profile, line 4, parallel to strike and directly over the body the anomaly is quite distinctive and clearly defines the location and extent of the conductor. Parallel lines not over the body, Figures 12e and 12f, show typical responses of quarter space models and do not show any effect of the nearby body. While these lines can be used to delineate the width of the body they also reveal the importance of closely spaced lines in detecting the body at all.

Reservoirs of significant dimension could easily be missed using the conventional approach of orienting dipole-dipole lines perpendicular to strike.

B. Down-Hole to Surface Resistivity Maps

Detailed delineation of subsurface conductivity distributions can often be effected by utilizing drill holes and a combination of surface and downhole electrodes. One such configuration involves lowering a current electrode down

the hole and measuring the voltages on the surface using orthogonal receiving electrode pairs (dipoles). The other current electrode is placed, effectively, at infinity. Quantitative analysis of this configuration has been limited to the case of single spheroidal bodies buried in a uniform half space, Merkel and Alexander (1971) Daniels (1977). For more comprehensive analysis it is necessary to include conductive overburden layers, faults, bounded near-surface inhomogenities, and arbitrary shapes of bodies. The three dimensional algorithm developed in this study is ideally suited for down-hole studies since there are no restrictions on the location of current sources, or in the definition of any arbitrary conductivity structures.

To illustrate the application of this technique we have analyzed the down hole to surface resistivity array for a simple tabular three-dimensional body.

The dimensions of this body and the coordinate axes are shown in the plan and section views of Figure 15. The resistivity of the tabular body is 1 ohm meter and that of the surrounding half space is 100 ohm m. Maps of apparent resistivity are made using the total electric fields obtained with orthogonal receiver dipoles on the surface. The maps encompass an area of 16 units in the x-direction by 14 units in the y-direction.

Figures 16 a,b,c, and d are the maps of total field apparent resistivities obtained with a current pole located at depths of 0.5, 1.0, 1.5 and 2.0 units, respectively, along a vertical line passing through the center of the body. When the electrode is above the body (Figure 16a) apparent resistivities close to that of the half space are observed near the hole. Within a radius of 2 units the values fall some 30%. At greater radii the values return to the half space resistivity. When the downhole electrode contacts the top of the body (Figure 16b) a pronounced low of 9 ohm-meters is observed over the center of the body. With increasing

distance away from the hole the apparent resistivities increase to the background values. For the case of the electrode within the body (Figure 16c) the central low increases to 23 ohm-meters and the values approach the half space values within a radius of 3 units. Finally, when the electrode is beneath the body the central low rises to 68 ohm-meters and a narrow annulus of anomalously high values (120 ohm-meters) encloses the surface projection of the body. With increasing radial distance from the hole the values rapidly approach the surrounding half space resistivity.

There is usually no difficulty in detecting a body if the drill hole passes through it. A more interesting case, therefore, is that of Figures 17, where the electrode is lowered down a hole located one unit away from the edge of the body. Figures 17 a,b,c,d, are the maps of total field apparent resistivities for an electrode buried at depths of 0.5, 1.0, 1.5, and 2.5 units respectively. In all of these maps a localized apparent resistivity high is observed in the vicinity of the hole. A zone of low values lies above the body and an arcuate zone of anomalously high values lies on the side of the body opposite the hole. Unlike the previous case, the maximum anomaly is now developed when the electrode is at the depth of the center of the body. The change in the anomaly amplitude and pattern as the current electrode moves from within the body to a point three units away from the edge of the body, at a depth of 1.5 units, is shown in Figures 16c, 18a (electrode contacting the left side of the body) and in Figures 17c and 18b, where the electrodes are 1 and 3 units away from the edge of the body, respectively. Even at three units distance the anomaly caused by the body is substantial (an Anomaly Index of approximately 80%) and the lateral position is well resolved in all cases. These results suggest that the array may be very useful in delineating conductive bodies missed in a drilling program. In this context, it is important to note that single profiles would not be as diagnostic

as the surface maps.

Figures 19 a, b, and c are maps of the total field apparent resistivity over a body of infinite strike length (in the y-direction). The cross section of body and its depth are identical to the three dimensional model used in the previous studies. The depths and locations of the current electrode are identical to those used in constructing the maps of Figures 16a, 16b and 17c respectively.

When the electrode is located centrally and above the body (Figure 19) the anomaly pattern is considerably different from that observed over the three dimensional body (Figure 16a). The apparent resistivity values are lower over the entire map area and, in fact, only reach the minimum value (25 ohm meters) at a radial distance of 5 units from the hole. As in the three dimensional case the maximum anomaly is produced when the electrode contacts the upper surface of the body (Figure 19b). In both Figures 19a and 19b the contours show the elongation in the y direction and in contrast to the three-dimensional case background values are not approached near the edge of the map.

When the electrode is located one unit away from the edge of the body and at a depth of 1.5 units (where the maximum anomaly occurrs) the two-dimensional body produces an apparent resistivity map (Figure 19c) quite distinct from the map of the corresponding three dimensional model (Figure 17c). In the two dimensional case an elongated low resistivity zone appears offset from the body on the side away from the current electrode. Surrounding half space resistivities are not approached within the confines of the map. In both cases a resistivity high occurs in the vicinity of the hole.

With a single hole ambiguities could arise between the anomalies produced by a uniform horizontal layer and those from a three dimensional body within the hole through its center. This ambiguity is removed with the data from a second hole. In this context, mise a la masse surveys are best conducted with an

electrode located off the axis of symmetry. Moreover the largest anomalies are produced when the electrode is in contact with the top or sides of the body rather than within the body.

Remarks

A general algorithm to simulate the response of an arbitrary three dimensional resistivity distribution to arbitrary arrays of current and receiver electrodes has been developed. We have illustrated the application of this algorithm with several simple models using both surface and downhole arrays. The finite difference mesh describing the conductive half space and the boundary conditions used make the algorithm easily amenable to the simulation of irregular topography. In addition, the apparent Induced Polarization response is readily obtained by assigning the intrinsic percent frequency effect to the resistivity of each elemental volume in the discretization process. Finally, the magnetometric resistivity response is easily calculated since the current flow in the lower space is derivable from the potentials at the nodes and the specified conductivities.

Acknowledgments

The authors are indebted to Mr. Juan C. Parra for his valuable assistance throughout this work. Support for this research has been provided by the United States Energy Research and Development Administration through Lawrence Berkeley Laboratory.

References

Bakbak, M.R., 1977, Three-Dimensional Numerical Modelling in Resistivity Prospecting, Ph.D. Thesis, University of California, Berkeley.

Coggon, J.H., 1971, Electromagnetic and Electrical Modelling by the Finite Element Method, Geophysics, vol. 36, p. 132.

Conens, P., and Golub, G.H., 1973, Use of fast direct methods for the efficient Numerical Solution of Non-Reparable Elliptic Equations, SIAM, J. Numer. Anal., vol. 10, p. 1103.

Daniels, J.J., 1977, Three-Dimensional Resistivity and Induced Polarization modelling using buried electrodes, Geophysics, vol. 42, p. 1006.

Dey, A., and Morrison, H.F., 1976, Resistivity modelling for arbitrarily shaped Two-Dimensional structures, Part I: Theoretical Formulation, Lawrence Berkeley Laboratory Report No. LBL-5223.

Dieter, K., Paterson, N.R., and Grant, F.S., 1969, IP and Resistivity type curves for Three-Dimensional bodies, Geophysics, vol. 34, p. 615.

Doss, S., 1977: Personal Communication.

Douglas, J.Jr., and Rockford, H.H.Jr., 1956, On the Numerical Solution of heat conduction problems in Two or Three space variables, Trans. Amer. Math. Soc., vol. 82, p. 421.

George, A., and Liu, J.W.H., 1976, An Automatic Nested Dissection Algorithm for Irregular Finite Element Problems, University of Waterloo, Canada,Research Report CS-76-38.

Gunn, J.E., 1964, The Numerical Solution of $\Delta.a\Delta u = f$ by a semi-explicit Alternating Direction Iterative Method, Numer. Math., vol. 6, p. 181.

Hestenes, M.R., and Stiefel, R., 1952, Method of Conjugate Gradients for solving Linear Systems: NBS, J. Res., vol. 49, p. 409.

Hohmann, G.N., 1975, Three-Dimensional induced Polarization and Electromagnetic modelling, Geophysics, vol. 40, p. 309.

Jepsen, A.F., 1969, Numerical Modelling in Resistivity Prospecting, Ph.D. Thesis, University of California, Berkeley.

Kershaw, D.S., 1976, The Incomplete Cholesky-Conjugate Gradient Method for the Iterative solution of Systems of Linear Equations, Lawrence Livermore Laboratory Report No. UERL-78333.

Lee, T., 1975, An Integral Equation and its Solution for some Two-and Three-Dimensional problems in resistivity and Induced Polarization, Geophys. J.R. Astro. Soc., vol. 42, p. 81.

McPhar Geophysics, 1966, Catalogue of Resistivity and IP Model Data, McPhar Geophysics Ltd, Ontario, Canada.

Madden, T.R., 1967, Calculations of Induced Polarization Anomalies for Arbitrary Two-Dimensional Resistivity Structure, Paper presented at Symposium on IP, University of California, Berkeley.

Meijerink, J.A., and Van Der Vorst, H.A., 1976, An Iterative Solution Method for Linear Systems of which the Coefficient Matrix is a symmetric M-matrix, Technical Report of TR-1, Academic Computer Center, Budapestlaan 6, de Uithof-Utrecht, The Netherlands.

Merkel, R.H., and Alexander, S.S., 1971, Resistivity Analysis for models of a sphere in a half-space with buried current sources, Geophys. Prosp., vol. 19, p. 640.

Meyer, W.H., 1977,, Computer Modeling of Electromagnetic Prospecting Methods, Ph.D. Thesis, University of California, Berkeley.

Reid, J.K., 1972, Two FORTRAN Subroutines for Direct Solution of Linear Equations whose matrix is sparse, symmetric and positive-definite, U.R.A.E.A. Research Group Report AERE-R7119.

Reid, J.K., Sparse Matrices, U.R.A.E.A. Computer Science and System Division Report no. CSS.31.

Sherman, A.H., 1975, Yale Sparse Matrix Packages, Lawrence Livermore Laboratory Report no. UCID-30114.

Southwell, R.V., 1946, Relaxation Methods in Theoretical Physics, vol. 1, Clarendon Press, Oxford.

Varga, R.S., 1962, Matrix Iterative Analysis, Prentice-Hall, Engleside Cliffs, New Jersey.

Wilson, E.L., Klaus-Jurgen, B., and Doherty, W.P., 1974, Direct solution of Large Systems of Linear Equations, Computers and Structures, vol. 4, p. 363.

Young, D., 1954, Iterative Methods for Solving Partial Differential Equations of Elliptic Type, Trans. Amer. Math. Soc., vol. 76, p. 92.

Zienkienicz, O.Z., 1971, Finite Element Method in Structural and Continuous Mechanics, McGraw-Hill, London.

Figures

Figure 12 Apparent resistivity pseudo-sections of the Basin and Range model along a) the profile line 1, b) the profile line 2, c) the profile line 3, d) the the profile line 4, e) the profile line 5, and f) the profile line 6 as indicated in the plan view.

Figure 13 Apparent resistivity pseudo-section of the two-dimensional Basin and Range model with no conductive reservoir zone near the fault.

Figure 14 Apparent resistivity pseudo-section of the two-dimensional Basin and Range model with the conductive reservoir zone.

Figure 15 Plan and sectional view of the test model used for the downhole to surface electrode configurations.

Figure 16 Maps of total field apparent resistivities with the current pole located along the vertical axis of the test model at depths of a) 0.5 units, b) 1.0 unit, c) 1.5 units, and d) 2.5 units below the surface.

Figure 17 Maps of total field apparent resistivities with the current pole located 1.0 units away from the edge of the test model at depths of a) 0.5 units, b) 1.0 unit, c) 1.5 units, and d) 2.5 units below the surface.

Figure 18 Maps of total field apparent resistivities with the current pole located at a depth of 1.5 units and a) 0.0 units and b) 3.0 units away from the edge of the test model.

Figure 19 Maps of total field apparent resistivities over the test model with infinite strike length with the current pole located along the vertical axis at depth of a) 0.5 units, b) 1.0 units, and c) with the current pole located 1.0 units away from the edge of the body at a depth of 1.5 units.

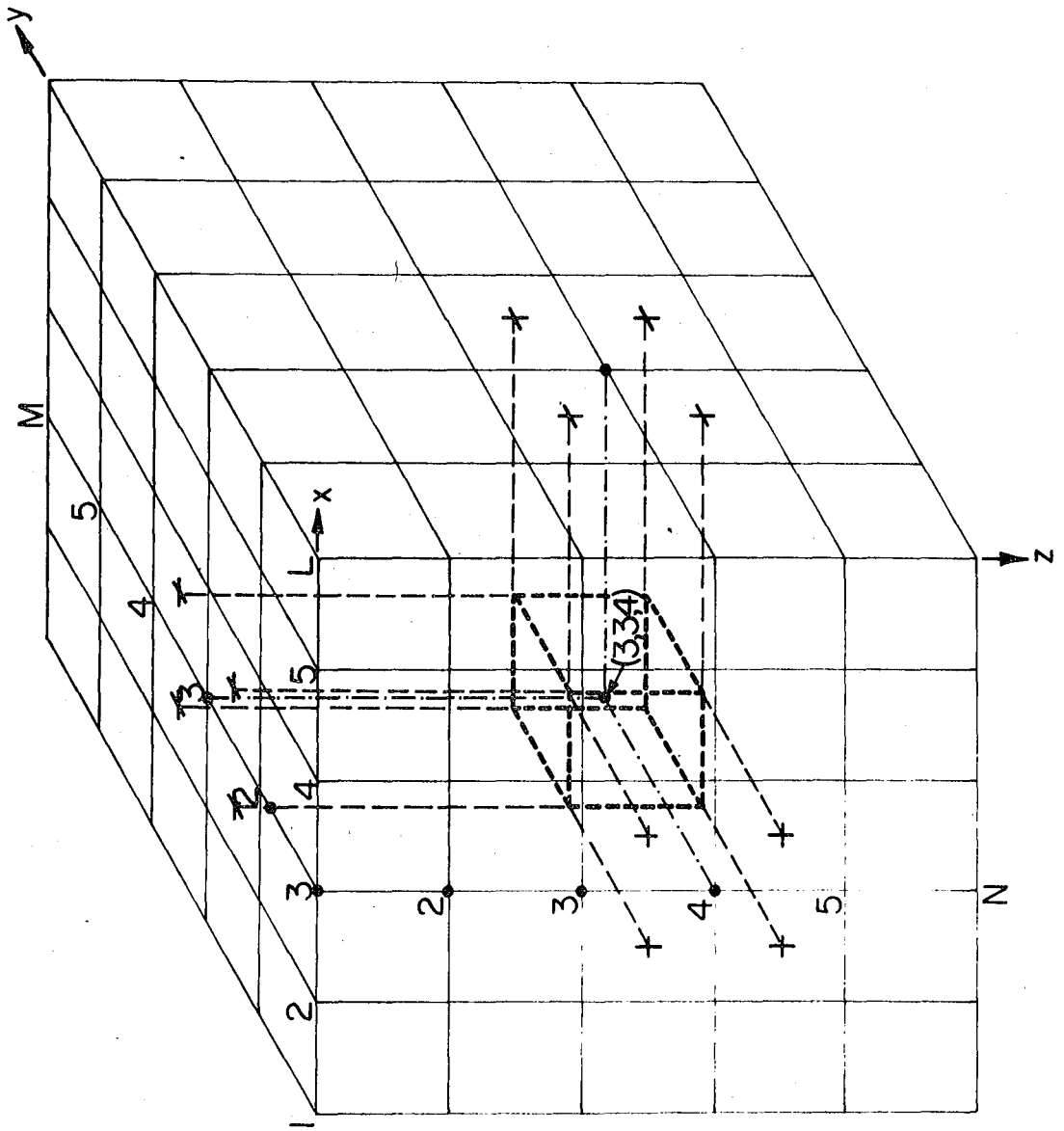

XBL7710-6158

Figure 1

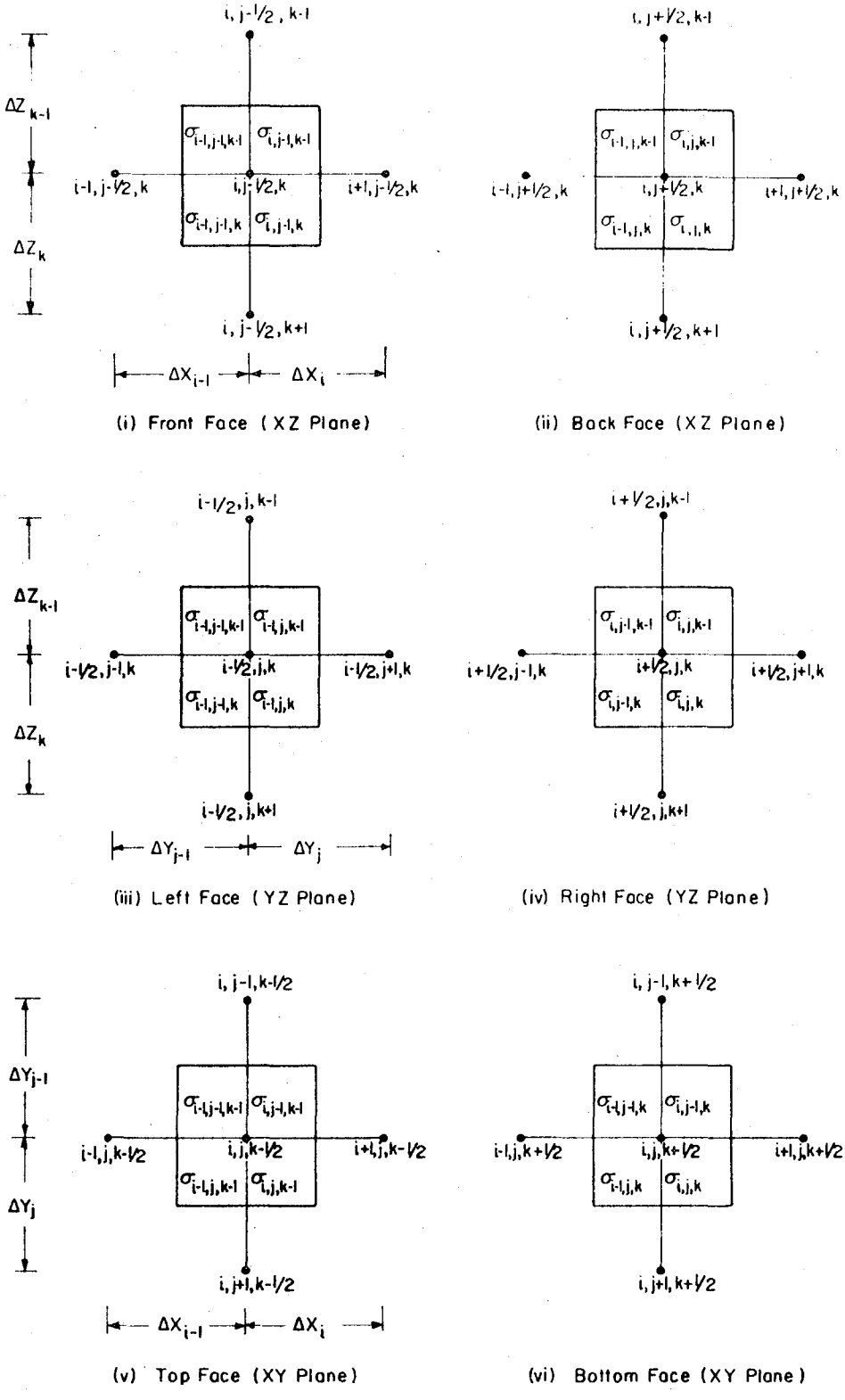

NODE LOCATIONS AND CONDUCTIVITY ON THE SIX SUBSURFACES OF $S_{i,j,k}$ ABOUT A NODE (i, j, k)

XBL 7710-6157

Figure 2

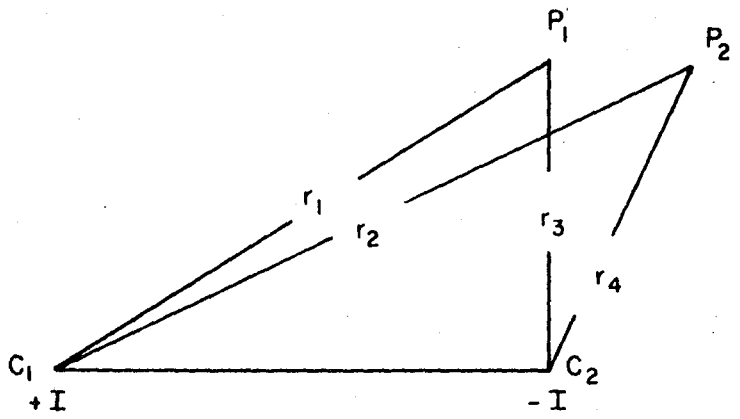

Figure 3

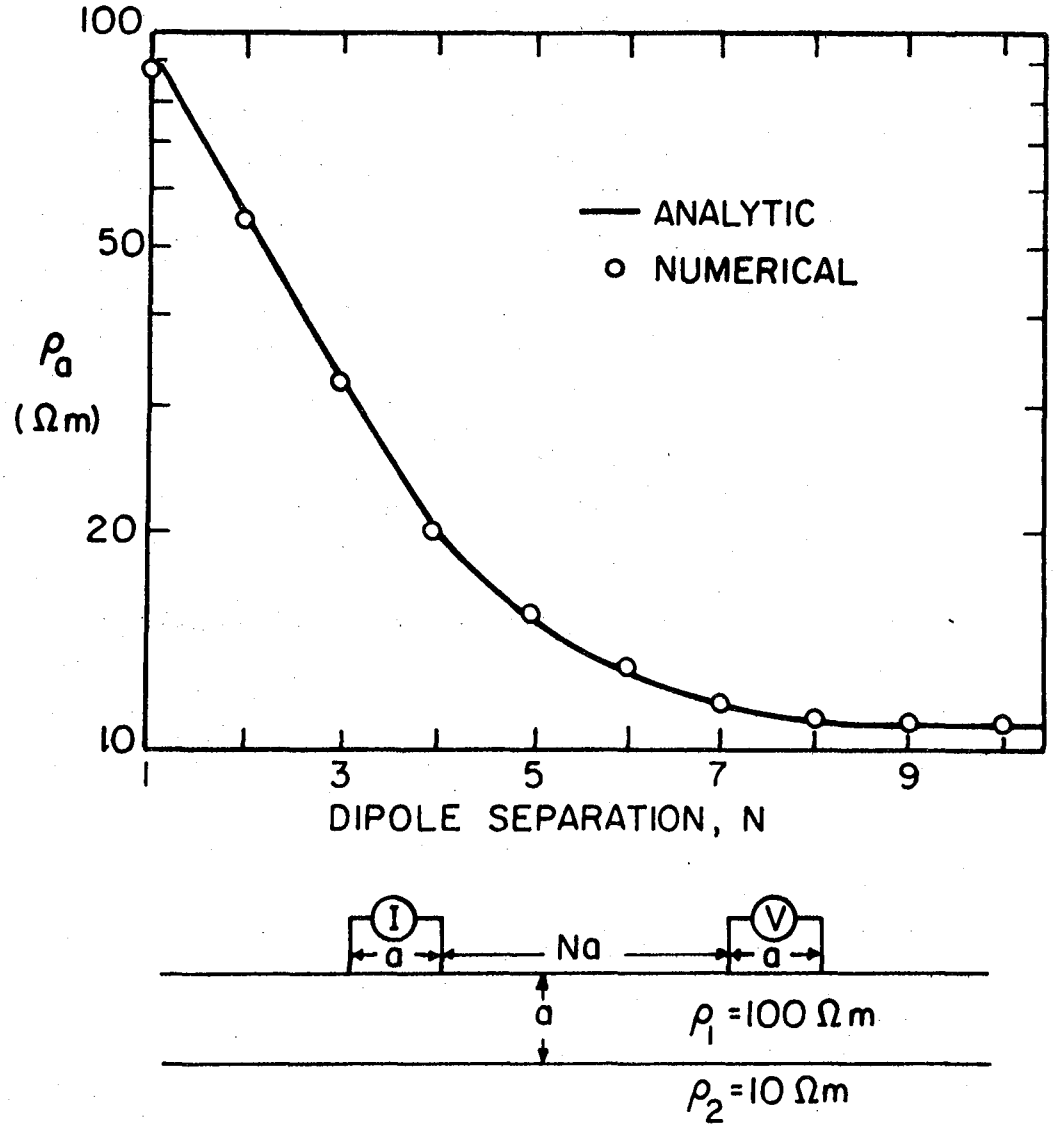
100
50
20
10
ρ_a
(Ωm)
ANALYTIC
NUMERICAL
1
3
5
7
9
DIPOLE SEPARATION, N
I
V
a
Na
a
a
ρ_1 = 100 Ωm
ρ_2 = 10 Ωm

Figure 4

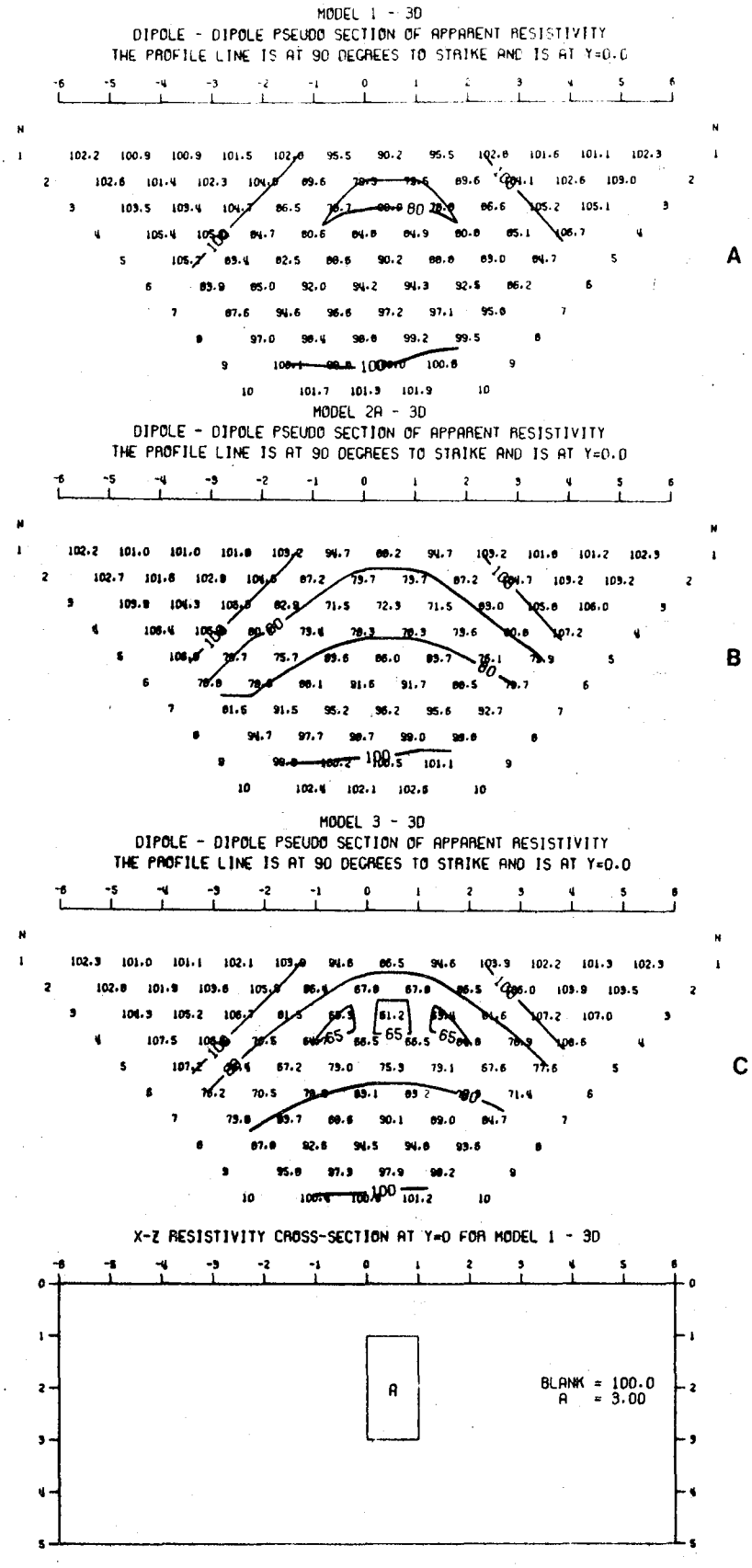
MODEL 1 - 3D
DIPOLE - DIPOLE PSEUDO SECTION OF APPARENT RESISTIVITY
THE PROFILE LINE IS AT 90 DEGREES TO STRIKE AND IS AT Y=0.0
A
MODEL 2A - 3D
DIPOLE - DIPOLE PSEUDO SECTION OF APPARENT RESISTIVITY
THE PROFILE LINE IS AT 90 DEGREES TO STRIKE AND IS AT Y=0.0
B
MODEL 3 - 3D
DIPOLE - DIPOLE PSEUDO SECTION OF APPARENT RESISTIVITY
THE PROFILE LINE IS AT 90 DEGREES TO STRIKE AND IS AT Y=0.0
C
X-Z RESISTIVITY CROSS-SECTION AT Y=0 FOR MODEL 1 - 3D
A
BLANK = 100.0
A = 3.00

Figure 5

MODEL 4 - 3D
DIPOLE - DIPOLE PSEUDO SECTION OF APPARENT RESISTIVITY
THE PROFILE LINE IS AT 90 DEGREES TO STRIKE AND IS AT Y=0.0

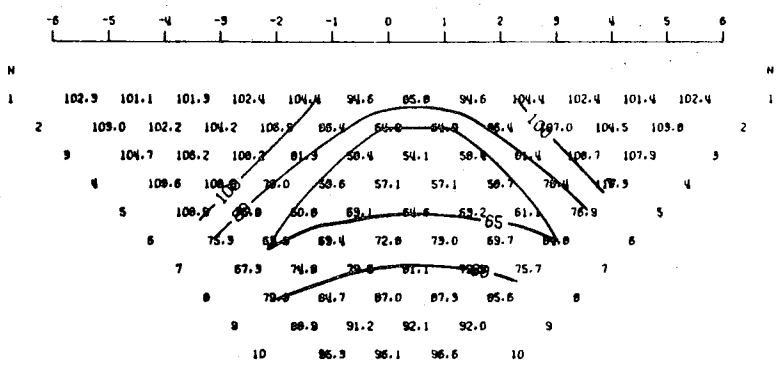

D

MODEL 5 - 3D
DIPOLE - DIPOLE PSEUDO SECTION OF APPARENT RESISTIVITY
THE PROFILE LINE IS AT 90 DEGREES TO STRIKE AND IS AT Y=0.0

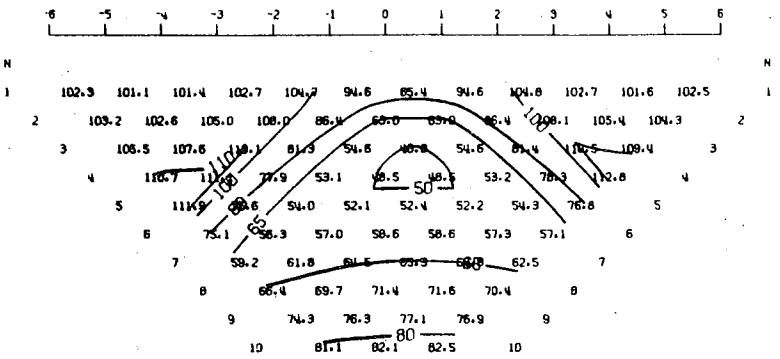

E

MODEL 5A - 2D
DIPOLE - DIPOLE PSEUDO SECTION OF APPARENT RESISTIVITY
THE PROFILE LINE IS AT 90 DEGREES TO STRIKE AND IS AT Y=0.0

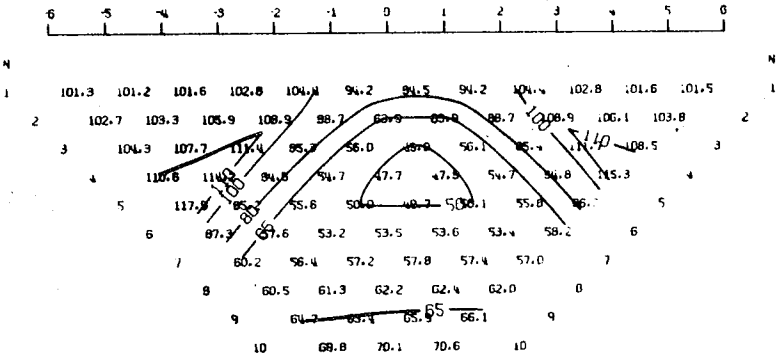

F

X-Z RESISTIVITY CROSS-SECTION AT Y=0 FOR MODEL 4 - 3D

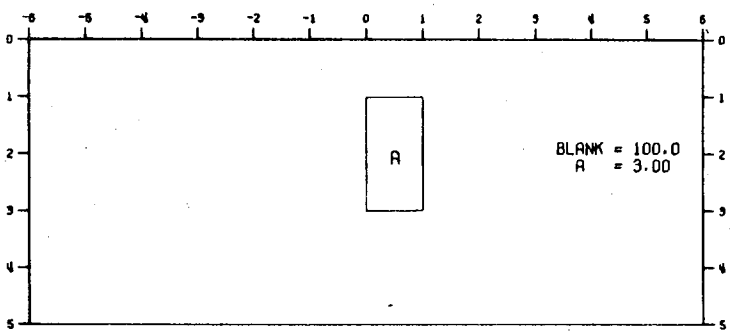

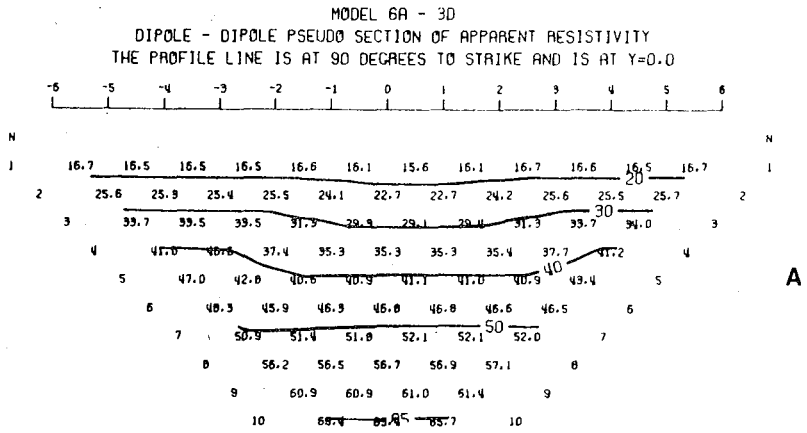
MODEL 6A - 3D
DIPOLE - DIPOLE PSEUDO SECTION OF APPARENT RESISTIVITY
THE PROFILE LINE IS AT 90 DEGREES TO STRIKE AND IS AT Y=0.0
A

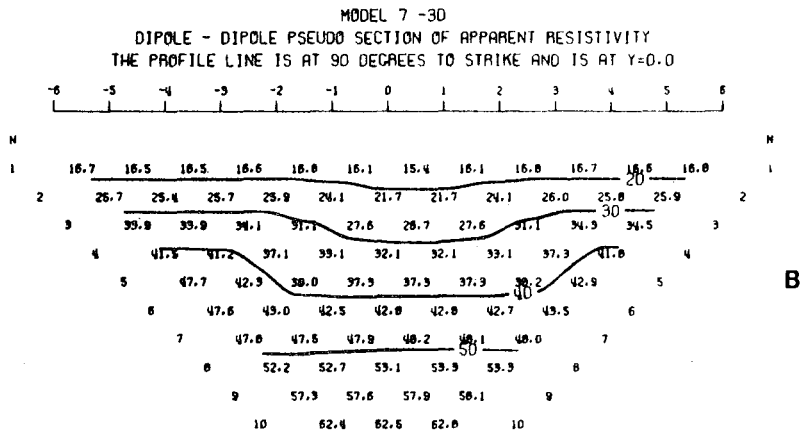
MODEL 7 -3D
DIPOLE - DIPOLE PSEUDO SECTION OF APPARENT RESISTIVITY
THE PROFILE LINE IS AT 90 DEGREES TO STRIKE AND IS AT Y=0.0
B

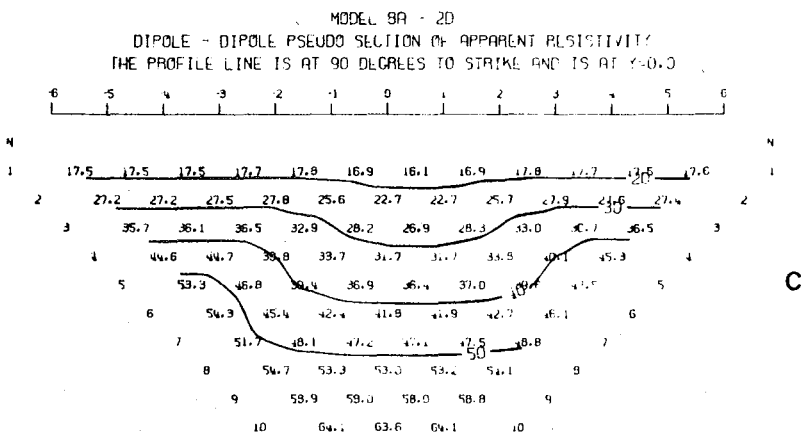
MODEL 8A - 2D
DIPOLE - DIPOLE PSEUDO SECTION OF APPARENT RESISTIVITY
THE PROFILE LINE IS AT 90 DEGREES TO STRIKE AND IS AT Y=0.0
C

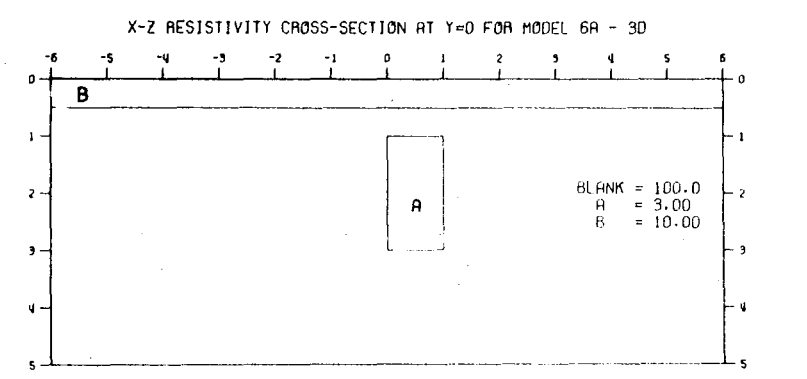
X-Z RESISTIVITY CROSS-SECTION AT Y=0 FOR MODEL 6A - 3D
B
A
BLANK = 100.0
A = 3.00
B = 10.00

Figure 6

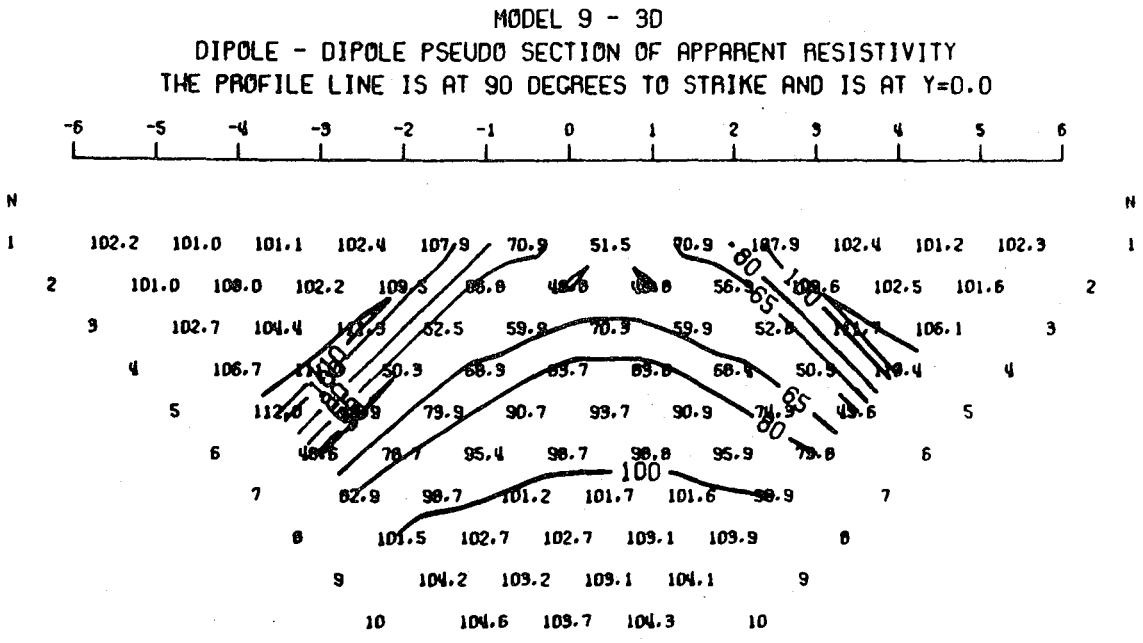
MODEL 9 - 3D
DIPOLE - DIPOLE PSEUDO SECTION OF APPARENT RESISTIVITY
THE PROFILE LINE IS AT 90 DEGREES TO STRIKE AND IS AT Y=0.0
-6 -5 -4 -3 -2 -1 0 1 2 3 4 5 6
N
1 102.2 101.0 101.1 102.4 107.9 70.9 51.5 70.9 107.9 102.4 101.2 102.3 1
2 101.0 108.0 102.2 109.5 56.6 108.6 102.5 101.6 2
3 102.7 104.4 52.5 59.8 70.3 59.9 52.6 106.1 3
4 106.7 50.3 68.3 69.7 68.4 50.5 4
5 79.9 90.7 93.7 90.9 5
6 95.4 98.7 98.8 95.9 6
7 98.7 101.2 101.7 101.6 98.9 7
8 101.5 102.7 102.7 103.1 103.9 8
9 104.2 103.2 103.1 104.1 9
10 104.6 103.7 104.3 10
60
65
100
80
100

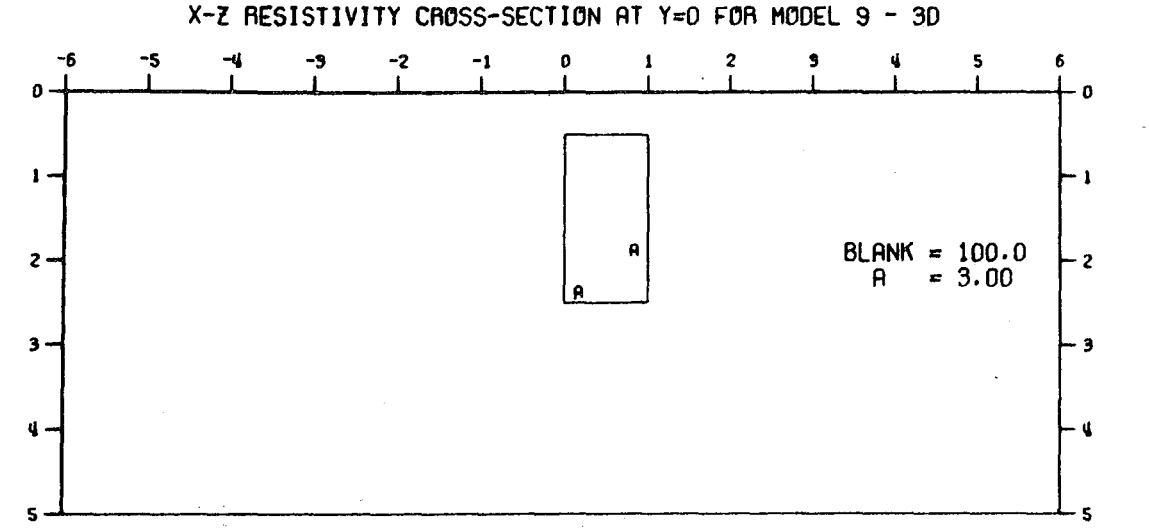
X-Z RESISTIVITY CROSS-SECTION AT Y=0 FOR MODEL 9 - 3D
-6 -5 -4 -3 -2 -1 0 1 2 3 4 5 6
0 1 2 3 4 5
A
A
BLANK = 100.0
A = 3.00

Figure 7

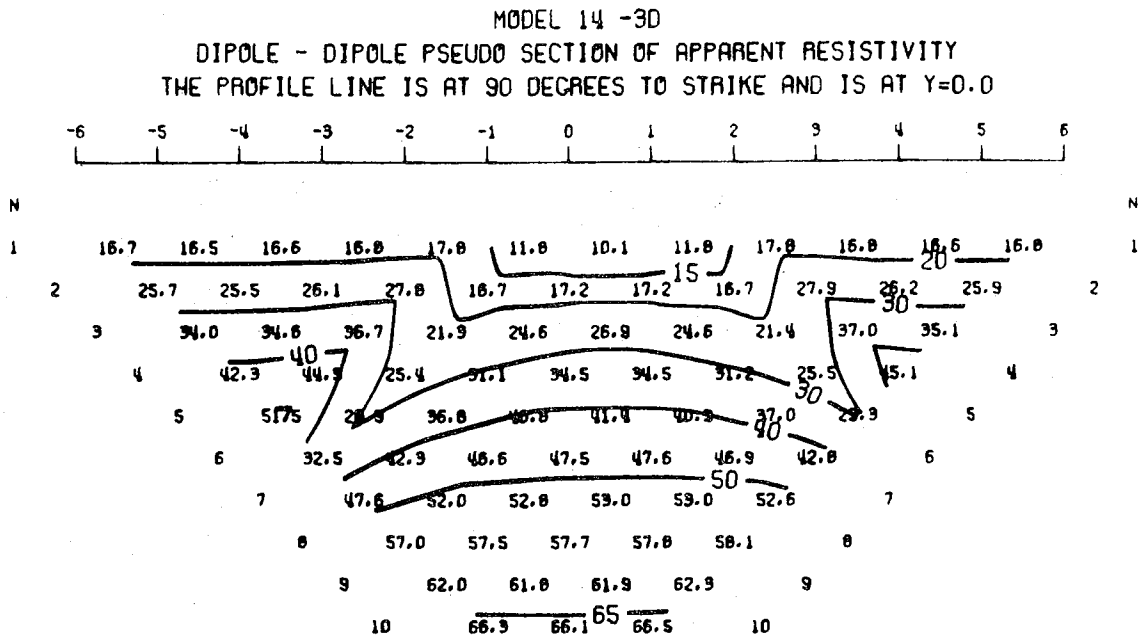
MODEL 14 -3D
DIPOLE - DIPOLE PSEUDO SECTION OF APPARENT RESISTIVITY
THE PROFILE LINE IS AT 90 DEGREES TO STRIKE AND IS AT Y=0.0
-6 -5 -4 -3 -2 -1 0 1 2 3 4 5 6
N
N
1 16.7 16.5 16.6 16.8 17.8 11.8 10.1 11.8 17.8 16.8 16.6 16.8 1
2 25.7 25.5 26.1 27.8 16.7 17.2 17.2 16.7 27.9 26.2 25.9 2
3 34.0 34.6 36.7 21.9 24.6 26.8 24.6 21.4 37.0 35.1 3
4 42.3 44.9 25.4 31.1 34.5 34.5 31.2 25.5 45.1 4
5 5175 36.8 40.8 41.4 40.3 37.0 29.9 5
6 32.5 42.9 46.6 47.5 47.6 46.9 42.8 6
7 47.6 52.0 52.8 53.0 53.0 52.6 7
8 57.0 57.5 57.7 57.8 58.1 8
9 62.0 61.8 61.9 62.9 9
10 66.9 66.1 66.5 10
15
20
30
40
30
40
50
65

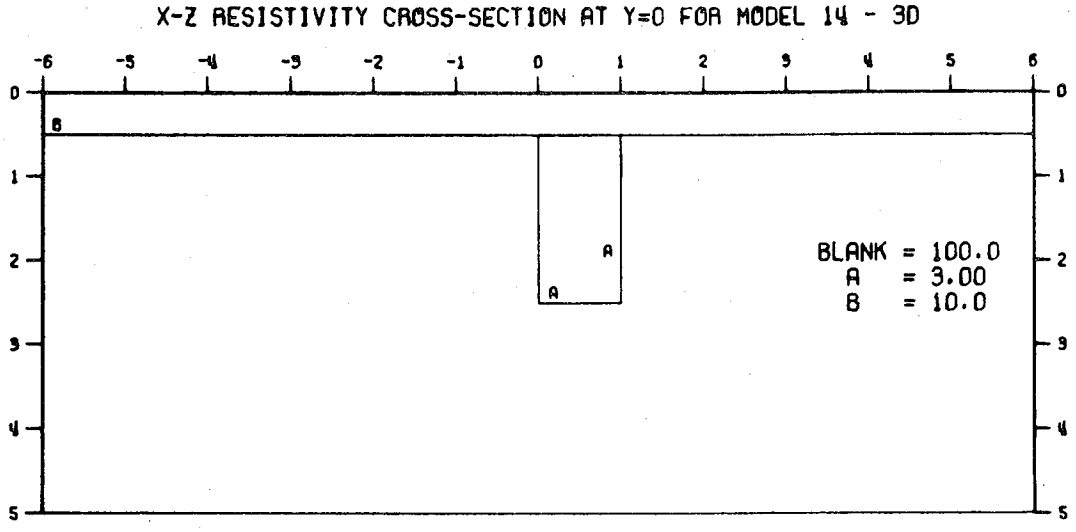
X-Z RESISTIVITY CROSS-SECTION AT Y=0 FOR MODEL 14 - 3D
-6 -5 -4 -3 -2 -1 0 1 2 3 4 5 6
0
1
2
3
4
5
B
A
A
BLANK = 100.0
A = 3.00
B = 10.0

Figure 8

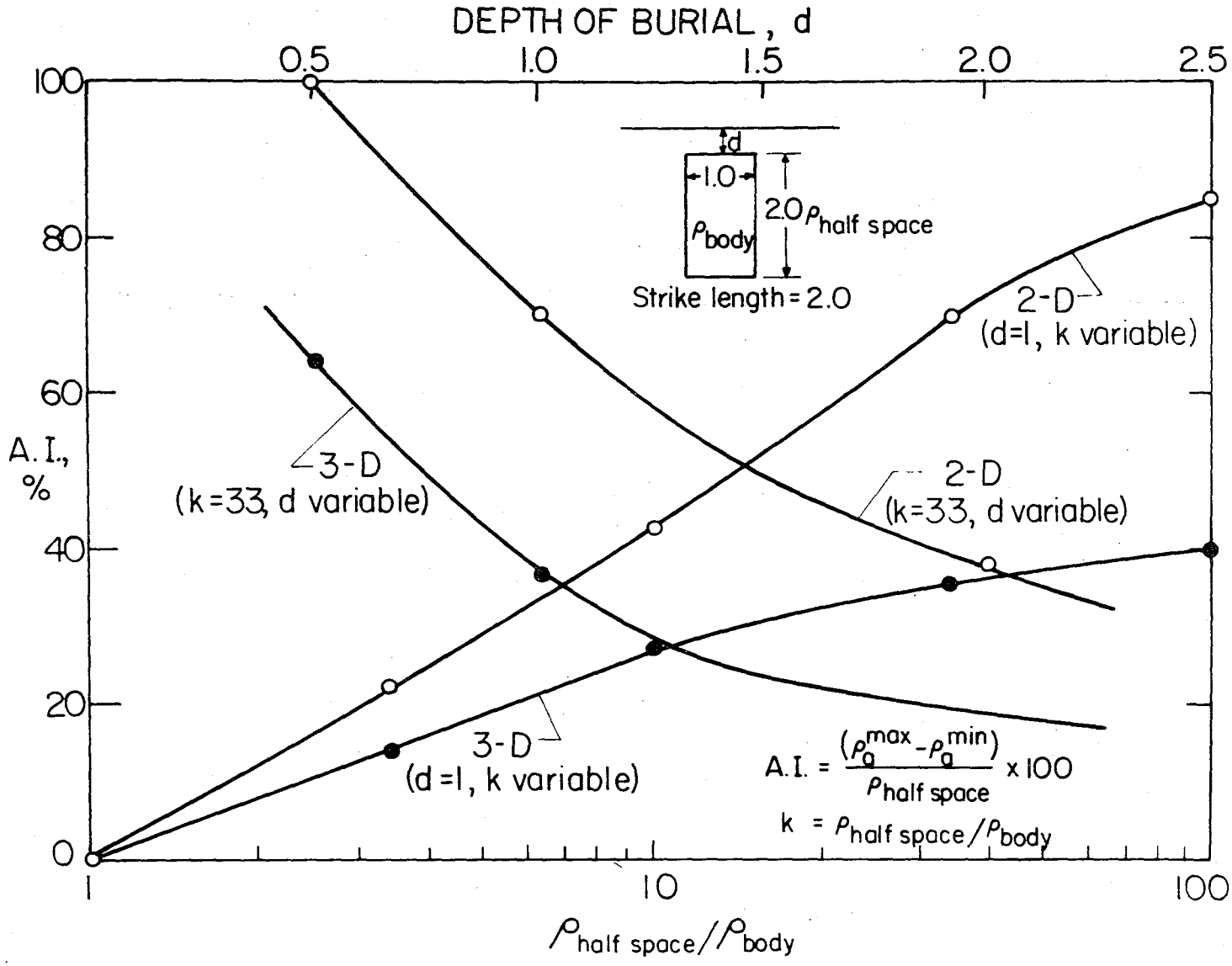
DEPTH OF BURIAL, d
0.5
1.0
1.5
2.0
2.5
100
80
60
40
20
0
A.I., %
d
1.0
ρ_{body}
$2.0\rho_{half\ space}$
Strike length = 2.0
2-D
(d=1, k variable)
3-D
(k=33, d variable)
2-D
(k=33, d variable)
3-D
(d=1, k variable)
$A.I. = \frac{(\rho_a^{max} - \rho_a^{min})}{\rho_{half\ space}} \times 100$
$k = \rho_{half\ space}/\rho_{body}$
1
10
100
$\rho_{half\ space}/\rho_{body}$

Figure 9

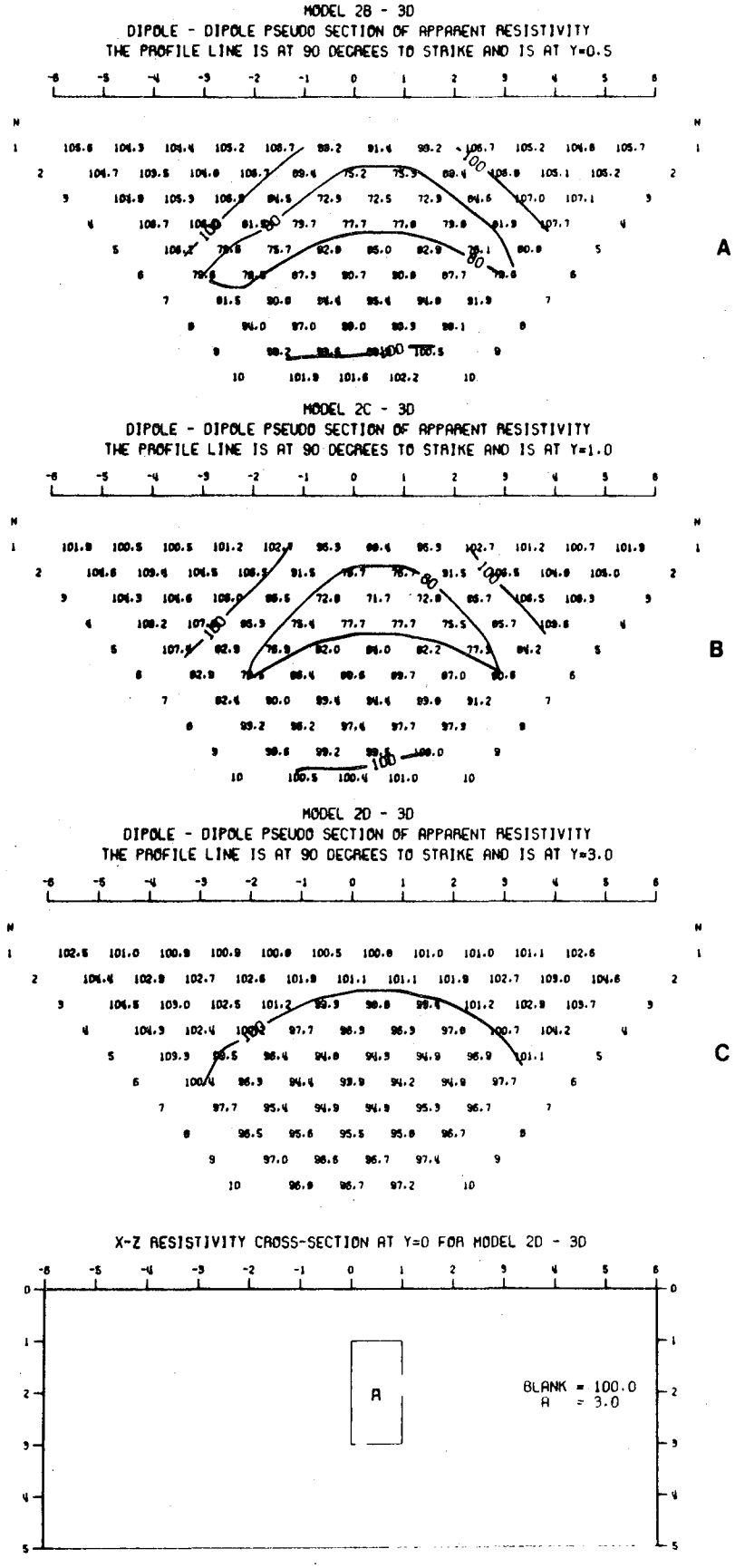
MODEL 2B - 3D
DIPOLE - DIPOLE PSEUDO SECTION OF APPARENT RESISTIVITY
THE PROFILE LINE IS AT 90 DEGREES TO STRIKE AND IS AT Y=0.5
A
MODEL 2C - 3D
DIPOLE - DIPOLE PSEUDO SECTION OF APPARENT RESISTIVITY
THE PROFILE LINE IS AT 90 DEGREES TO STRIKE AND IS AT Y=1.0
B
MODEL 2D - 3D
DIPOLE - DIPOLE PSEUDO SECTION OF APPARENT RESISTIVITY
THE PROFILE LINE IS AT 90 DEGREES TO STRIKE AND IS AT Y=3.0
C
X-Z RESISTIVITY CROSS-SECTION AT Y=0 FOR MODEL 2D - 3D
A
BLANK = 100.0
A = 3.0

Figure 10

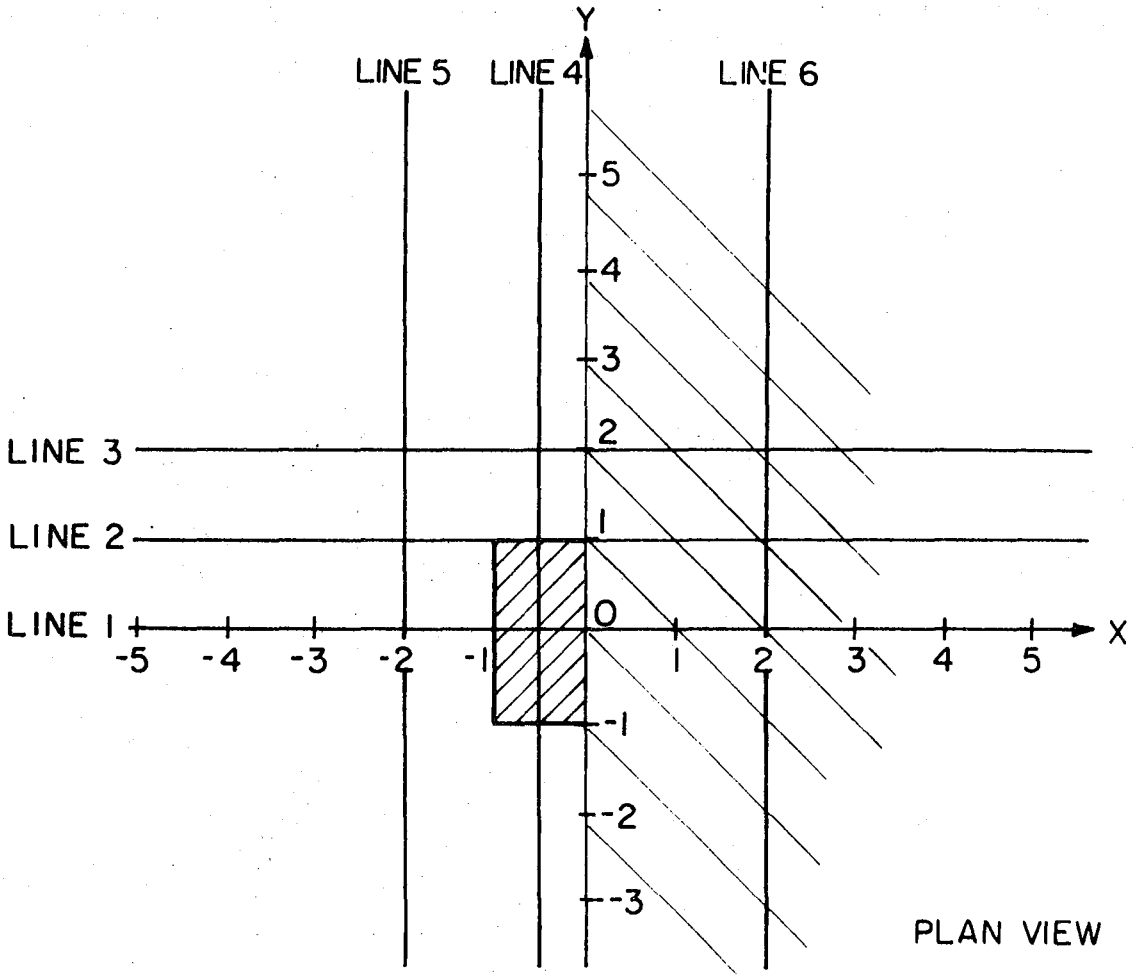
Y
LINE 5
LINE 4
LINE 6
5
4
3
2
1
0
-1
-2
-3
LINE 3
LINE 2
LINE 1
-5 -4 -3 -2 -1 1 2 3 4 5
X
PLAN VIEW

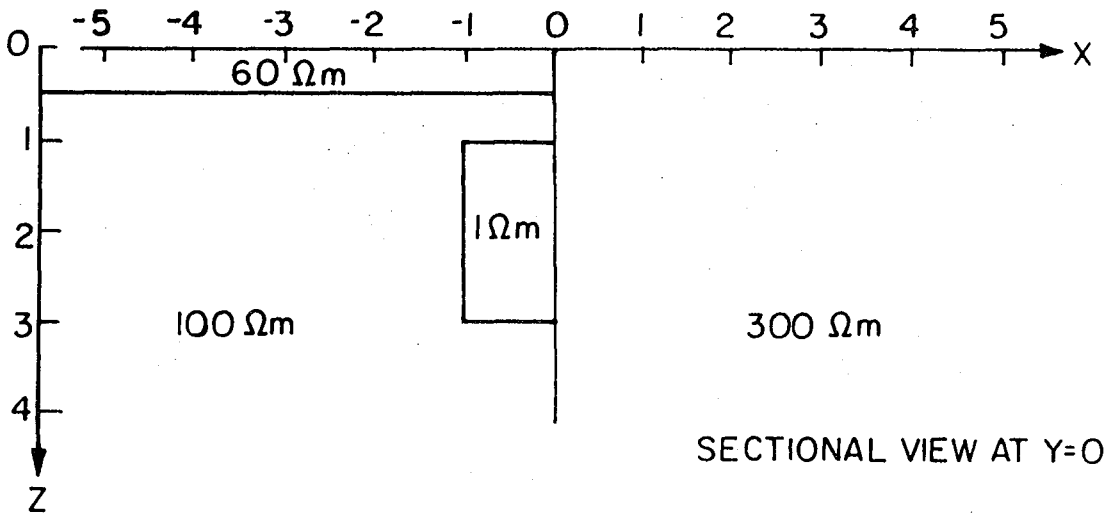
-5 -4 -3 -2 -1 0 1 2 3 4 5
X
0
60 Ωm
1
2
3
4
1Ωm
100 Ωm
300 Ωm
Z
SECTIONAL VIEW AT Y=0

Figure 11

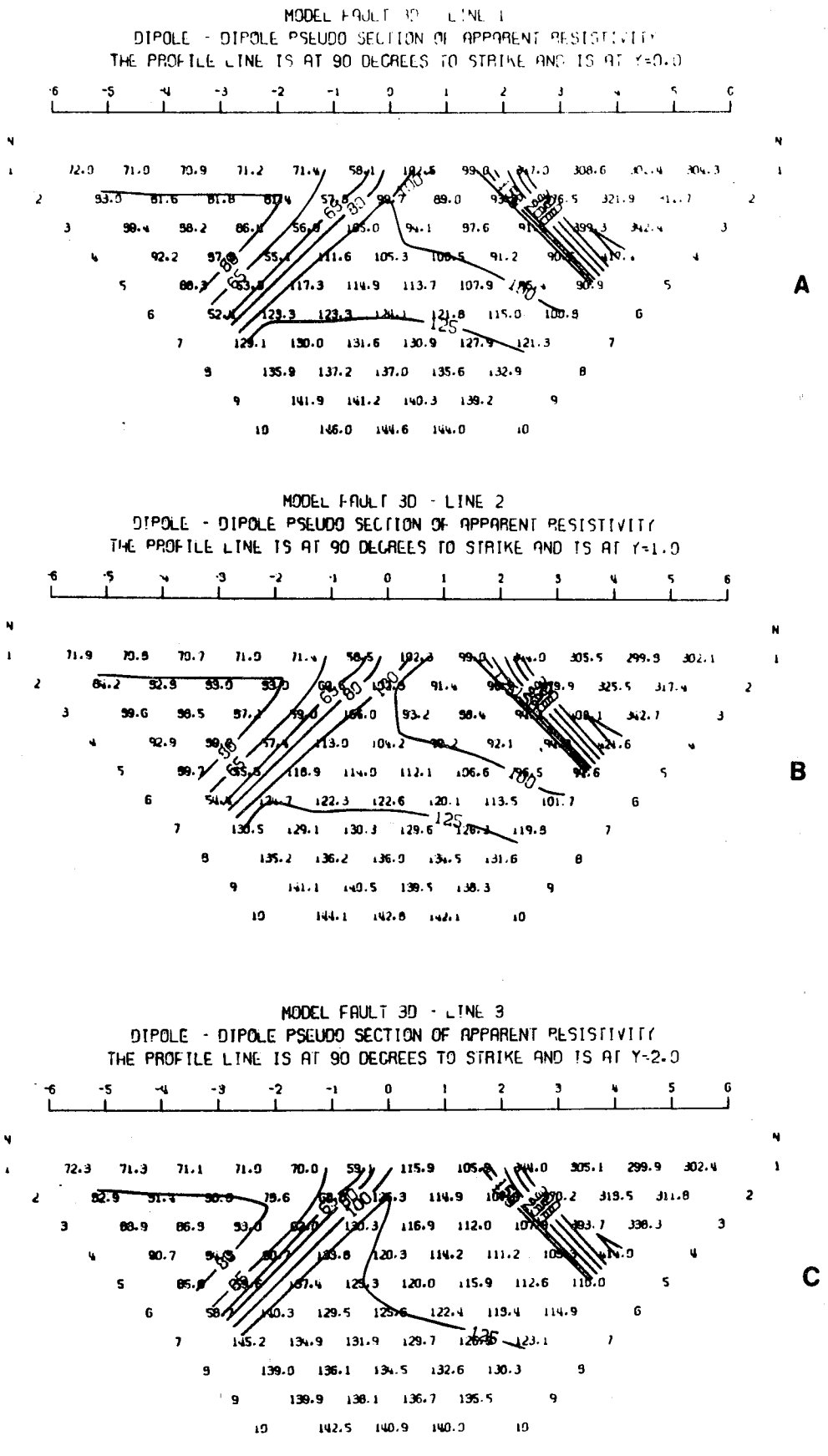
MODEL FAULT 3D - LINE 1
DIPOLE - DIPOLE PSEUDO SECTION OF APPARENT RESISTIVITY
THE PROFILE LINE IS AT 90 DEGREES TO STRIKE AND IS AT Y=0.0
MODEL FAULT 3D - LINE 2
DIPOLE - DIPOLE PSEUDO SECTION OF APPARENT RESISTIVITY
THE PROFILE LINE IS AT 90 DEGREES TO STRIKE AND IS AT Y=1.0
MODEL FAULT 3D - LINE 3
DIPOLE - DIPOLE PSEUDO SECTION OF APPARENT RESISTIVITY
THE PROFILE LINE IS AT 90 DEGREES TO STRIKE AND IS AT Y=2.0
A
B
C

Figure 12

MODEL FAULT 3D - LINE 4
DIPOLE - DIPOLE PSEUDO SECTION OF APPARENT RESISTIVITY
THE PROFILE LINE IS AT 0 DEGREES TO STRIKE AND IS AT X=-0.5

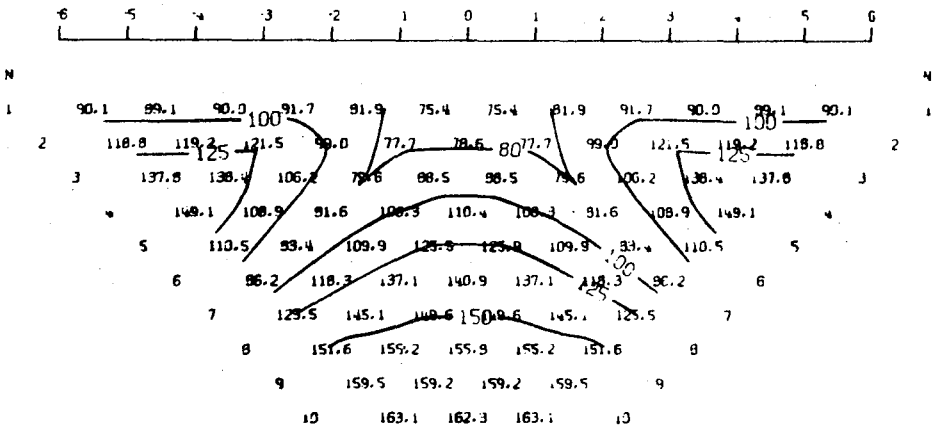

MODEL FAULT 3D - LINE 5
DIPOLE - DIPOLE PSEUDO SECTION OF APPARENT RESISTIVITY
THE PROFILE LINE IS AT 0 DEGREES TO STRIKE AND IS AT X=-2.0

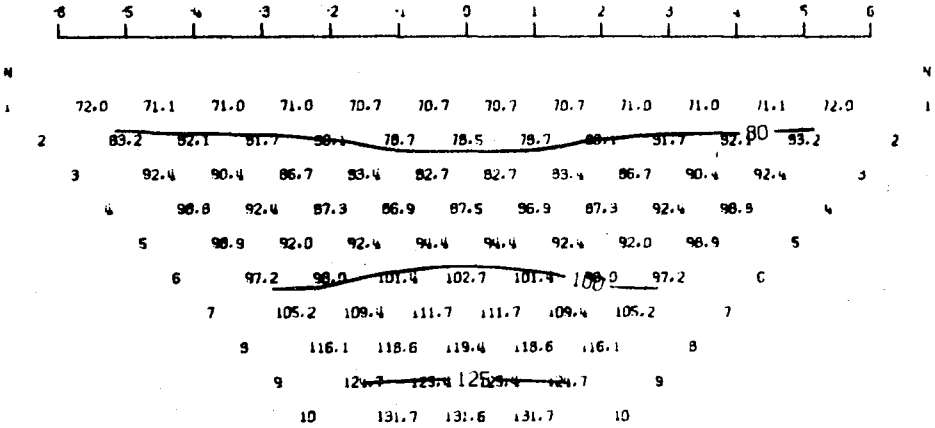

MODEL FAULT 3D - LINE 6
DIPOLE - DIPOLE PSEUDO SECTION OF APPARENT RESISTIVITY
THE PROFILE LINE IS AT 0 DEGREES TO STRIKE AND IS AT X=+2.0

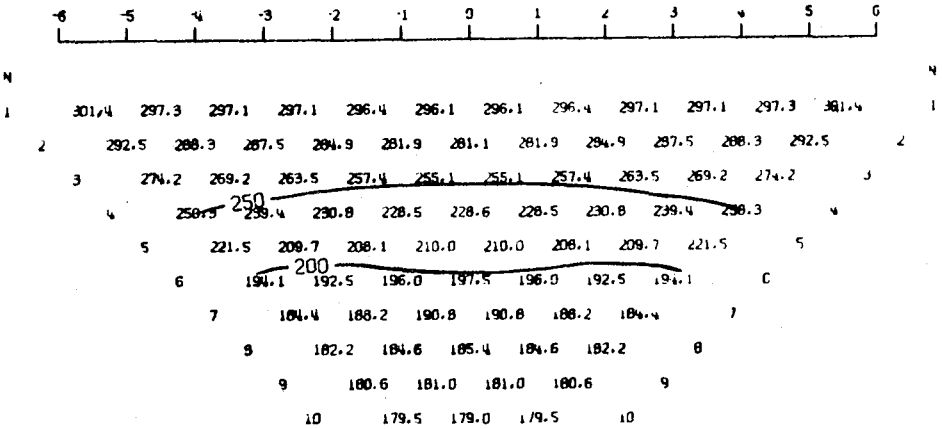

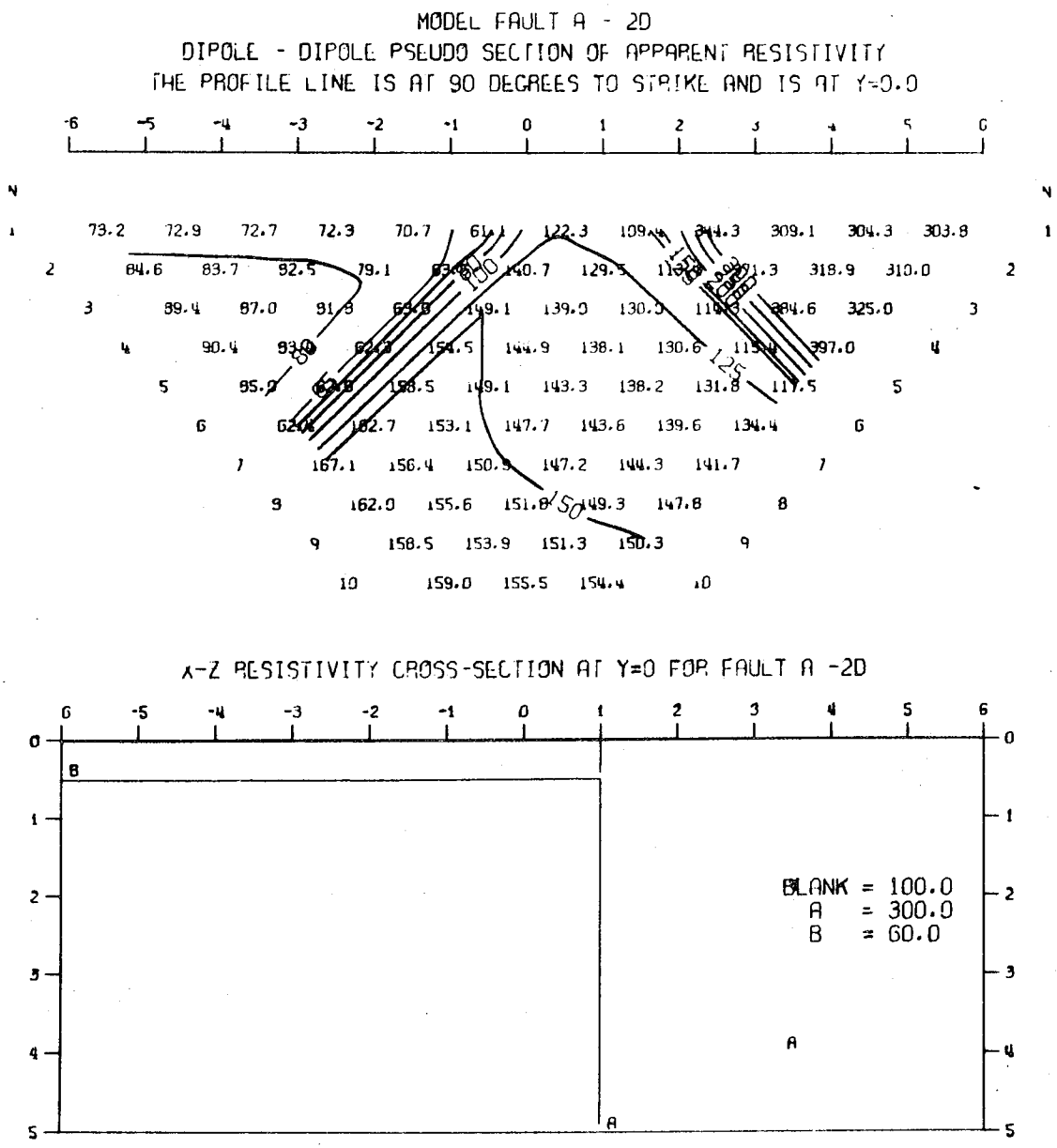
MODEL FAULT A - 2D
DIPOLE - DIPOLE PSEUDO SECTION OF APPARENT RESISTIVITY
THE PROFILE LINE IS AT 90 DEGREES TO STRIKE AND IS AT Y=0.0
-6 -5 -4 -3 -2 -1 0 1 2 3 4 5 6
N
73.2 72.9 72.7 72.3 70.7 122.3 309.1 304.3 303.8
84.6 83.7 82.5 79.1 140.7 129.5 318.9 310.0
89.4 87.0 149.1 139.0 130.5 325.0
90.4 154.5 144.9 138.1 130.6 397.0
95.0 158.5 149.1 143.3 138.2 131.8 117.5
162.7 153.1 147.7 143.6 139.6 134.4
167.1 156.4 150.9 147.2 144.3 141.7
162.0 155.6 151.8 149.3 147.8
158.5 153.9 151.3 150.3
159.0 155.5 154.4
X-Z RESISTIVITY CROSS-SECTION AT Y=0 FOR FAULT A -2D
BLANK = 100.0
A = 300.0
B = 60.0
A
B

Figure 13

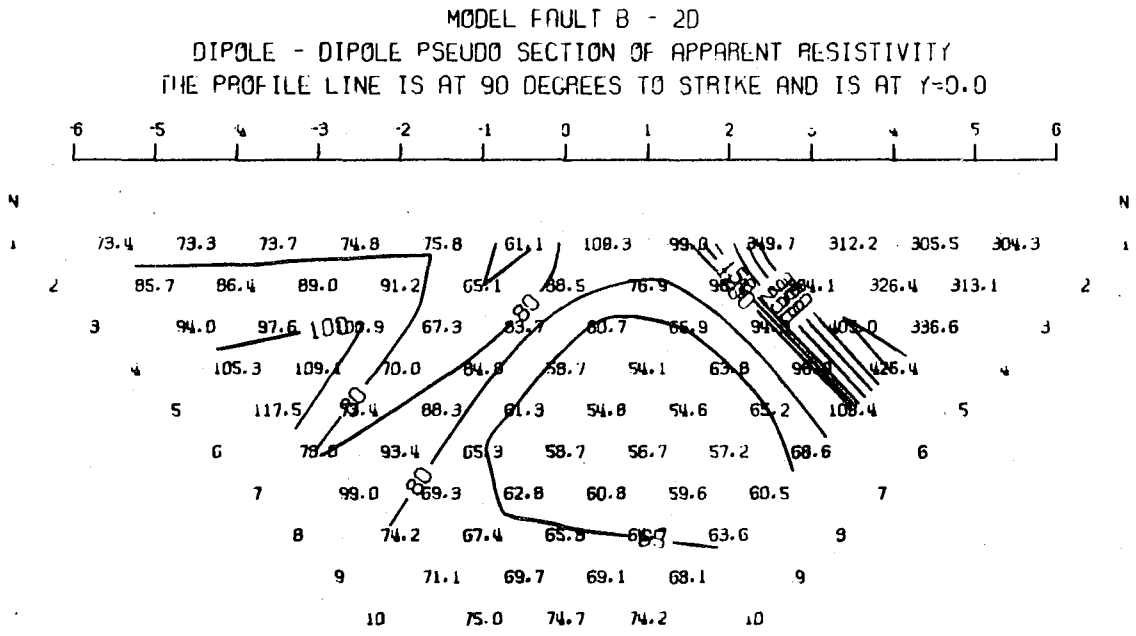
MODEL FAULT B - 2D
DIPOLE - DIPOLE PSEUDO SECTION OF APPARENT RESISTIVITY
THE PROFILE LINE IS AT 90 DEGREES TO STRIKE AND IS AT Y=0.0
-6 -5 -4 -3 -2 -1 0 1 2 3 4 5 6
N
1 73.4 73.3 73.7 74.8 75.8 61.1 108.3 99.0 319.7 312.2 305.5 304.3
2 85.7 86.4 89.0 91.2 65.1 88.5 76.9 326.4 313.1
3 94.0 97.6 100 67.3 80.7 66.9 336.6
4 105.3 109.1 70.0 58.7 54.1 63.8 426.4
5 117.5 88.3 61.3 54.8 54.6 65.2 108.4
6 78.8 93.4 58.7 56.7 57.2 68.6
7 99.0 69.3 62.8 60.8 59.6 60.5
8 74.2 67.4 63.6
9 71.1 69.7 69.1 68.1
10 75.0 74.7 74.2
80
80
80
100
150
200
250
300

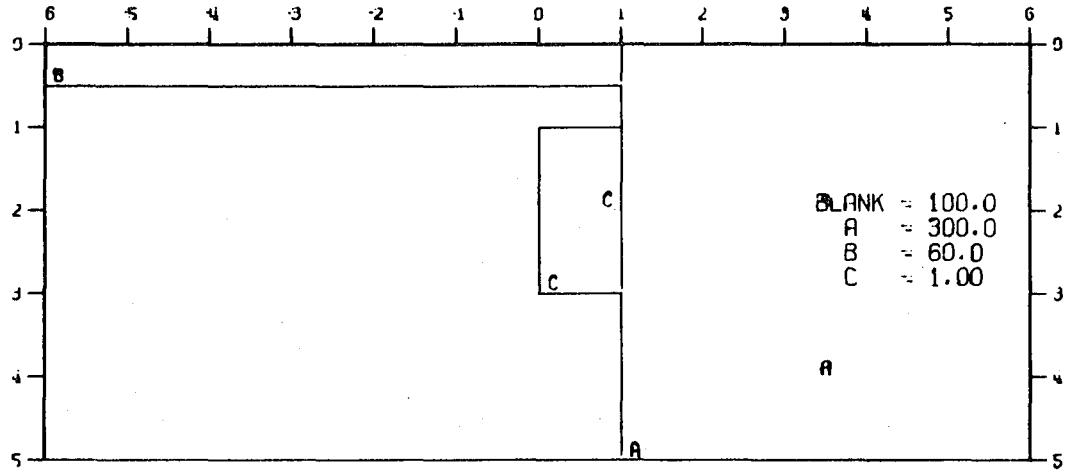
X-Z RESISTIVITY CROSS-SECTION AT Y=0 FOR FAULT B -2D
6 5 4 3 2 1 0 1 2 3 4 5 6
0 1 2 3 4 5
B
C
C
A
A
BLANK = 100.0
A = 300.0
B = 60.0
C = 1.00

Figure 14

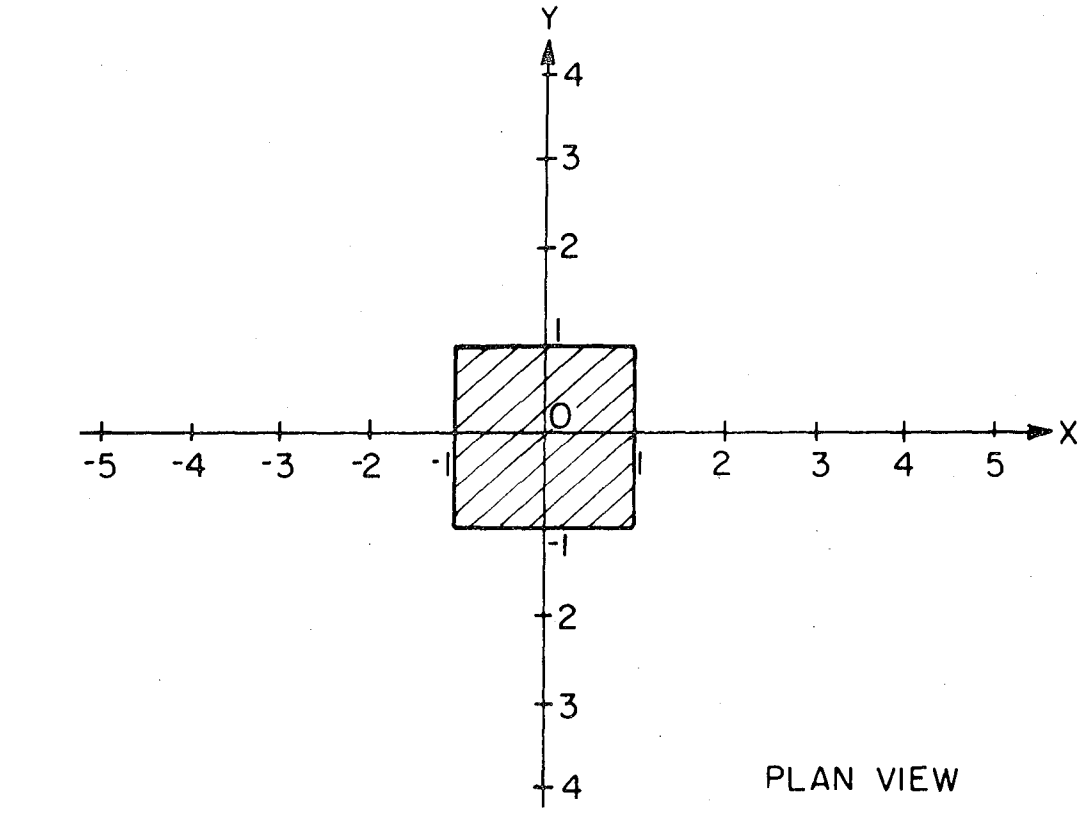
Y
4
3
2
1
0
X
-5
-4
-3
-2
-1
1
2
3
4
5
-1
2
3
4
PLAN VIEW

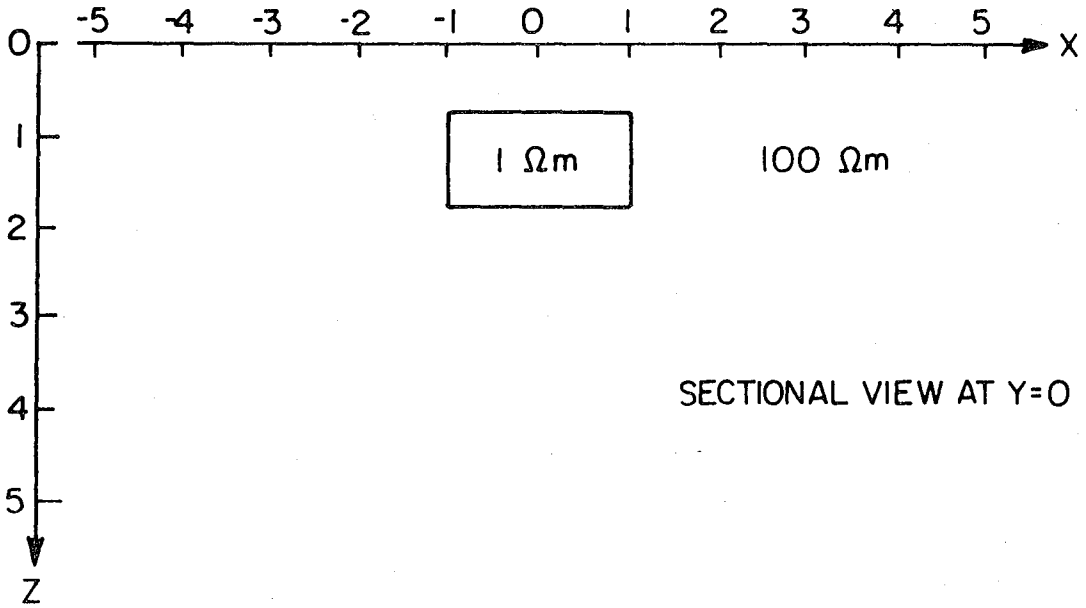
-5
-4
-3
-2
-1
0
1
2
3
4
5
X
0
1
2
3
4
5
Z
1 Ωm
100 Ωm
SECTIONAL VIEW AT Y=0

Figure 15

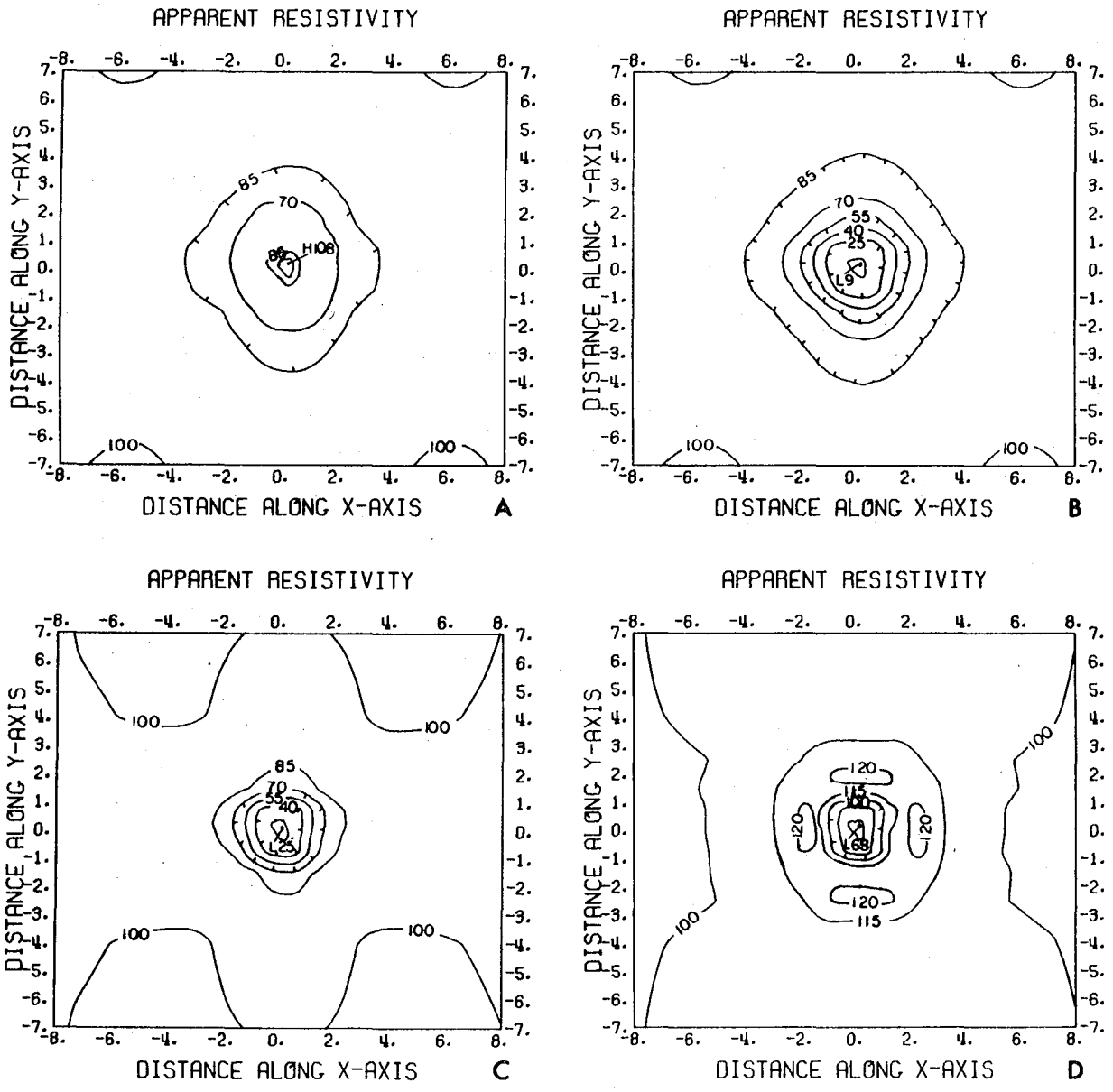
APPARENT RESISTIVITY
DISTANCE ALONG Y-AXIS
DISTANCE ALONG X-AXIS
A
APPARENT RESISTIVITY
DISTANCE ALONG Y-AXIS
DISTANCE ALONG X-AXIS
B
APPARENT RESISTIVITY
DISTANCE ALONG Y-AXIS
DISTANCE ALONG X-AXIS
C
APPARENT RESISTIVITY
DISTANCE ALONG Y-AXIS
DISTANCE ALONG X-AXIS
D

Figure 16

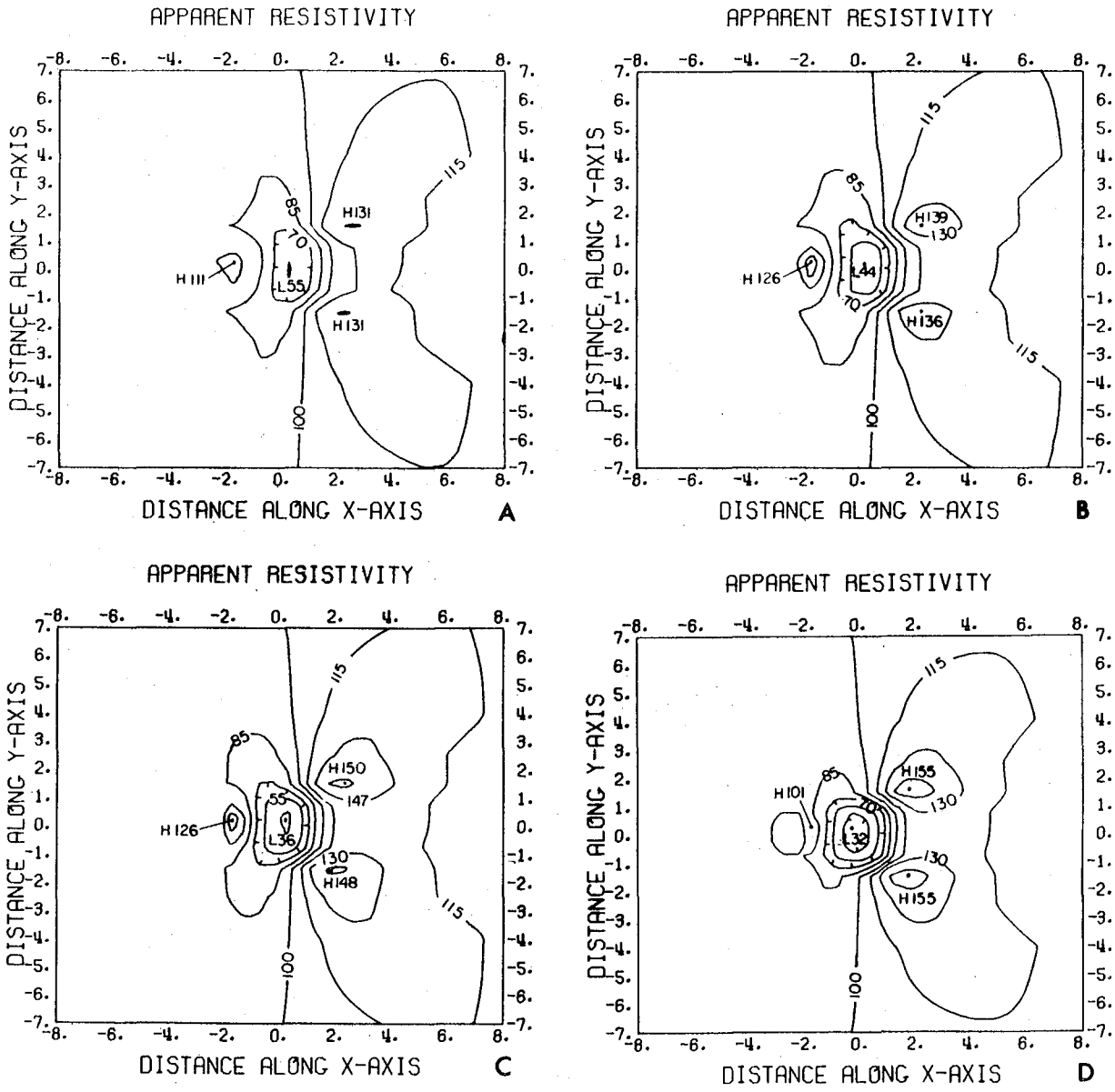
APPARENT RESISTIVITY
DISTANCE ALONG Y-AXIS
DISTANCE ALONG X-AXIS
A
H111
L55
H131
H131
85
70
115
100
APPARENT RESISTIVITY
DISTANCE ALONG Y-AXIS
DISTANCE ALONG X-AXIS
B
H126
L44
H139
130
H136
85
70
115
100
APPARENT RESISTIVITY
DISTANCE ALONG Y-AXIS
DISTANCE ALONG X-AXIS
C
H126
L36
H150
147
H148
130
85
55
115
100
APPARENT RESISTIVITY
DISTANCE ALONG Y-AXIS
DISTANCE ALONG X-AXIS
D
H101
L32
H155
130
H155
130
85
70
115
100

Figure 17

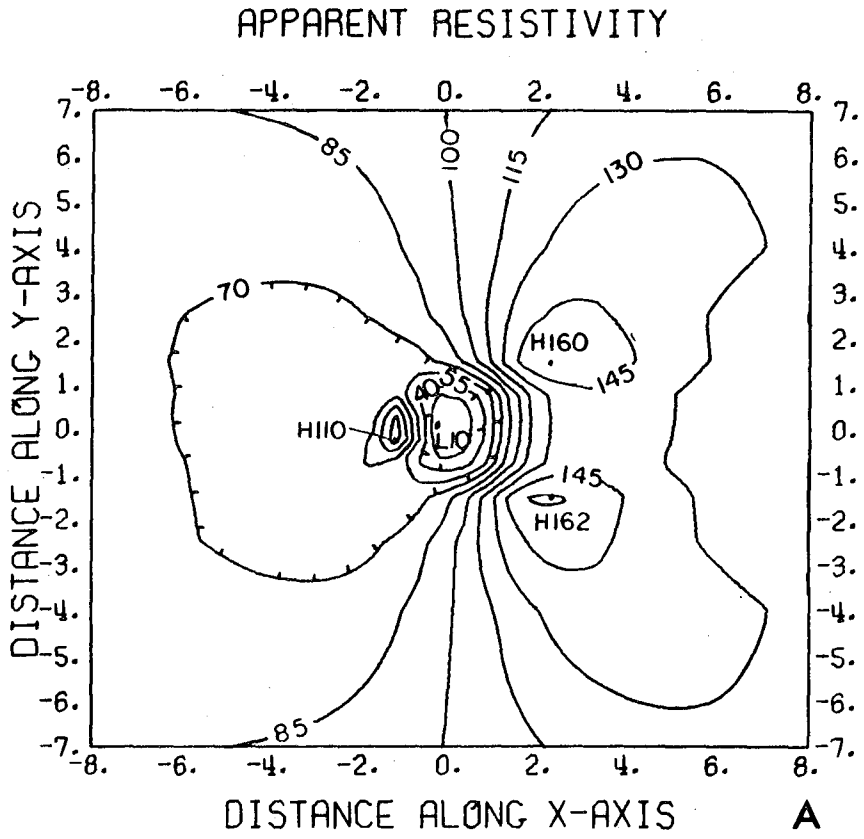
APPARENT RESISTIVITY
DISTANCE ALONG Y-AXIS
DISTANCE ALONG X-AXIS
A
85
100
115
130
70
H160
145
H110
L10
145
H162
85

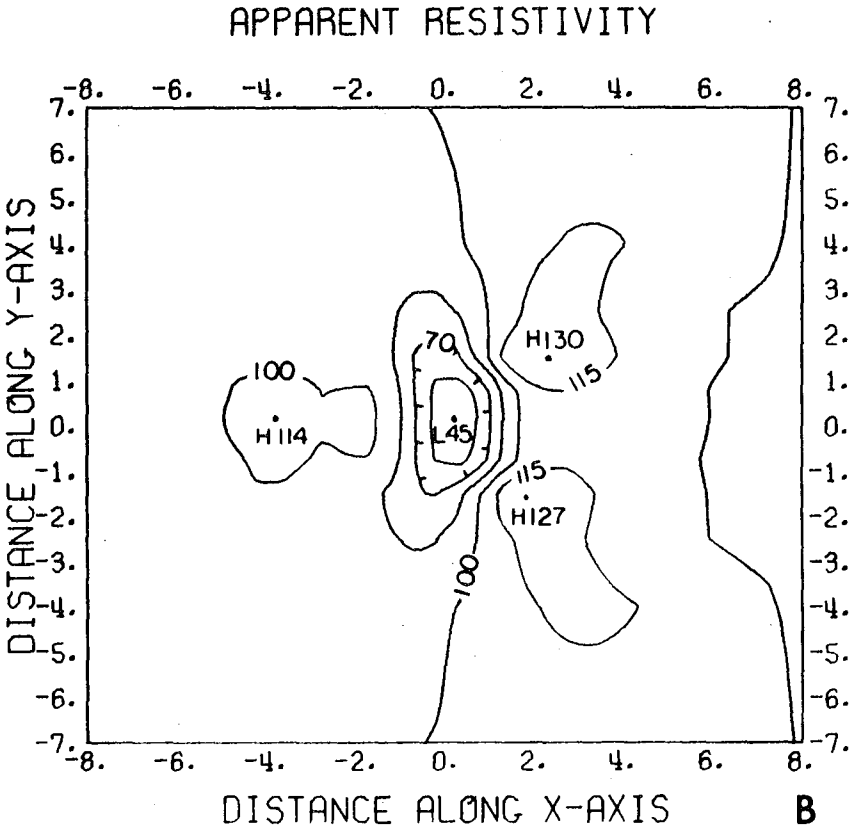
APPARENT RESISTIVITY
DISTANCE ALONG Y-AXIS
DISTANCE ALONG X-AXIS
B
100
H114
70
L45
H130
115
115
H127
100

Figure 18

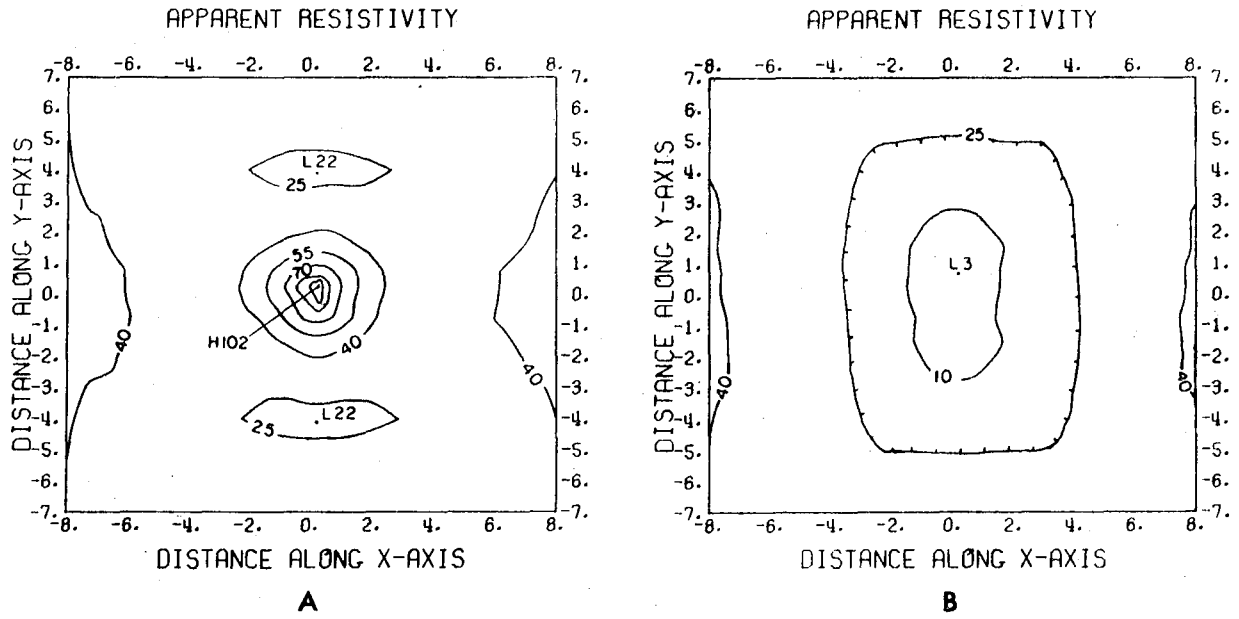
APPARENT RESISTIVITY
DISTANCE ALONG Y-AXIS
DISTANCE ALONG X-AXIS
L22
25
55
70
H102
40
L22
25
A
APPARENT RESISTIVITY
DISTANCE ALONG Y-AXIS
DISTANCE ALONG X-AXIS
25
L3
10
40
B

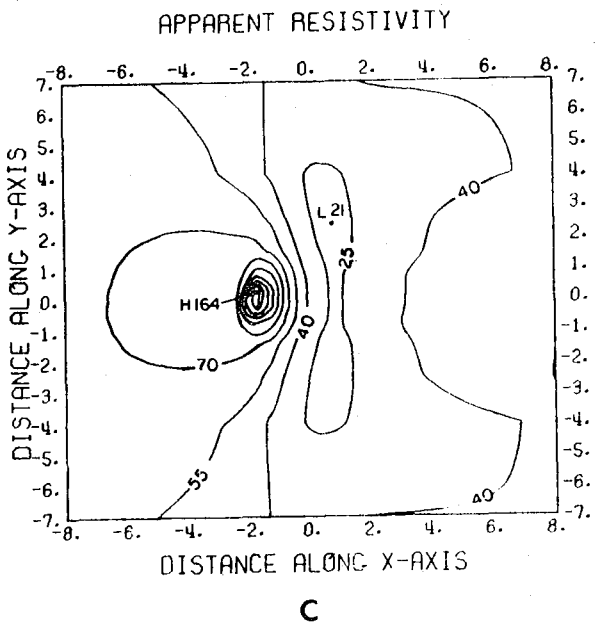
APPARENT RESISTIVITY
DISTANCE ALONG Y-AXIS
DISTANCE ALONG X-AXIS
L21
25
40
H164
70
55
40
C

Figure 19

This report was done with support from the United States Energy Research and Development Administration. Any conclusions or opinions expressed in this report represent solely those of the author(s) and not necessarily those of The Regents of the University of California, the Lawrence Berkeley Laboratory or the United States Energy Research and Development Administration.